REPORT DOCUMENTATION PAGE

Form Approved
OMB No. 0704-0188

1. REPORT DATE *(DD-MM-YYYY)*	**2. REPORT TYPE**	**3. DATES COVERED** *(From - To)*
January 2014	Journal Article	January 2014-February 2014

4. TITLE AND SUBTITLE

Boron Nanoparticles with High Hydrogen Loading: Mechanism for B-H Binding, Size Reduction, and Potential for Improved Combustibility and Specific Impulse

5a. CONTRACT NUMBER
In-House

5b. GRANT NUMBER

5c. PROGRAM ELEMENT NUMBER

6. AUTHOR(S)

Jesus Paulo L. Perez, Brandon W. McMahon, Jiang Yu, Stefan Schneider, Jerry A. Boatz, Tom W. Hawkins, Parker D. McCrary, Luis A. Flores, Robin D. Rogers, and Scott L. Anderson

5d. PROJECT NUMBER

5e. TASK NUMBER

5f. WORK UNIT NUMBER
Q0RA

7. PERFORMING ORGANIZATION NAME(S) AND ADDRESS(ES)

Air Force Research Laboratory (AFMC)
AFRL/RQRP
10 E. Saturn Blvd.
Edwards AFB, CA, 93524-7680

8. PERFORMING ORGANIZATION REPORT NO.

9. SPONSORING / MONITORING AGENCY NAME(S) AND ADDRESS(ES)

Air Force Research Laboratory (AFMC)
AFRL/RQR
5 Pollux Drive.
Edwards AFB, CA, 93524-7048

10. SPONSOR/MONITOR'S ACRONYM(S)

11. SPONSOR/MONITOR'S REPORT NUMBER(S)
AFRL-RQ-ED-JA-2014-035

12. DISTRIBUTION / AVAILABILITY STATEMENT
Approved for public release; distribution unlimited

13. SUPPLEMENTARY NOTES
Journal article published in the ACS Nano, Vol. #6, Issue #11 May 2014.
PA Case Number: #14090; Clearance Date: 24 Feb 14.

14. ABSTRACT

Ball milling of boron in an H2 atmosphere was found to result in hydrogen uptake of up to 5 % by weight (36 mole %). The nature of the hydrogen binding to boron was probed by a combination of *ab initio* theory, IR spectroscopy, thermogravimetric analysis, and mass spectral measurements of gases evolved during sample heating. The dominant binding mode is found to be H atoms bound to B atoms in the surface layer of the particles, and the high hydrogen loading results from production of very high surface area, indicating that gaseous H2 is an effective agent promoting size reduction in milling. Hydrogen incorporated in the samples was found to be stable for at least a month under ambient conditions. Desorption is observed beginning at ~60 °C and continuing as the temperature is increased, with broad desorption features peaking at ~250 °C and ~450 °C, and ending at ~800 °C. Unprotected hydrogenated boron nanoparticles were found to be reactive with O2 producing a hydrated boron oxide surface layer that decomposed readily at 100 °C leading to desorption of H2O. Hydrogenated boron nanoparticles were found to promote a higher flame height in the hypergolic ignition of ionic liquids upon contact with nitric acid.

15. SUBJECT TERMS

16. SECURITY CLASSIFICATION OF:			**17. LIMITATION OF ABSTRACT**	**18. NUMBER OF PAGES**	**19a. NAME OF RESPONSIBLE PERSON**
					Stefan Schneider
a. REPORT	**b. ABSTRACT**	**c. THIS PAGE**			**19b. TELEPHONE NO** *(include area code)*
Unclassified	**Unclassified**	**Unclassified**	SAR	75	661-275-5759

Standard Form 298 (Rev. 8-98)
Prescribed by ANSI Std. 239.18

Boron Nanoparticles with High Hydrogen Loading: Mechanism for B−H Binding, Size Reduction, and Potential for Improved Combustibility and Specific Impulse

Jesus Paulo L. Perez[†], Brandon W. McMahon[†], Jiang Yu[†], Stefan Schneider[‡a], Jerry A. Boatz[‡a], Tom W. Hawkins[‡a], Parker D. McCrary[§], Luis A. Flores[§], Robin D. Rogers[§a], and Scott L. Anderson[†a]*

[†] Department of Chemistry, University of Utah, 315 S 1400 E, Salt Lake City, UT 84112, USA

[‡] Propellants Branch, Rocket Propulsion Division, Aerospace Systems Directorate, Air Force Research Laboratory, AFMC AFRL/RQRP, 10 E Saturn Blvd, Edwards AFB, CA 93524, USA

[§] Center for Green Manufacturing and Department of Chemistry, The University of Alabama, Tuscaloosa, AL 35487, USA

Abstract

Ball milling of boron in an H_2 atmosphere was found to result in hydrogen uptake of up to 5 % by weight (36 mole %). The nature of the hydrogen binding to boron was probed by a combination of *ab initio* theory, IR spectroscopy, thermogravimetric analysis, and mass spectral measurements of gases evolved during sample heating. The dominant binding mode is found to be H atoms bound to B atoms in the surface layer of the particles, and the high hydrogen loading results from production of very high surface area, indicating that gaseous H_2 is an effective agent promoting size reduction in milling. Hydrogen incorporated in the samples was found to be stable for at least a month under ambient conditions. Desorption is observed beginning at ~60 °C and continuing as the temperature is increased, with broad desorption features peaking at ~250 °C and ~450 °C, and ending at ~800 °C. Unprotected hydrogenated boron nanoparticles were found to be reactive with O_2 producing a hydrated boron oxide surface layer that decomposed readily at 100 °C leading to desorption of H_2O. Hydrogenated boron nanoparticles were found to promote a higher flame height in the hypergolic ignition of ionic liquids upon contact with nitric acid.

[*]Corresponding Author [a]Senior Author

Keywords: hydrogen enrichment, boron, mass spectroscopy, energetic materials

Boron's high heat of combustion makes it an interesting material for fuel and propellant applications.[1] Boron is quite refractory, thus combustion is inherently a heterogeneous process, limited by the surface area of the boron particles. Reduction of boron into the nanoscale can, therefore, improve combustibility,[2-4] however formation of a refractory oxide layer on the particle surfaces upon air exposure impedes ignition and reduces the energy density. One approach to mitigating the effects of the oxide layer is to cap nanoparticulate boron with organic capping ligands, which protect the boron from premature oxidation, and control dispersibility in fuels/propellants.[5-8] Here, we examine a different approach to improving boron's potential as a propellant – production of boron nanoparticles containing up to 5 weight percent of hydrogen (~36 mole percent). Incorporation of hydrogen may have several effects. By reducing the average molecular weight of the combustion products, the specific impulse (I_{sp}) would be improved, all else being equal.[7] In addition, given the fact that boranes (B_nH_m compounds) tend to be highly reactive with oxidizers,[9] hydrogenation of boron might be expected to increase reactivity. Given its low atomic mass and propensity for making compounds with hydrogen, boron also has potential as a hydrogen storage material.[10] For example, diborane (B_2H_6) is 22 wt% hydrogen, surpassed only by methane (CH_4, 25 wt%) in hydrogen content.

Hydrogen loading and adsorption properties of nanostructured solid boron compounds such as BN[11,12] and MgB_2[11] have been studied recently. Tang et al.[11] measured as much as 5.6 wt% hydrogen loading on mesoporous BN nanotubes, while Pecharsky et al.[11] were able to load ~4 wt% hydrogen into powdered MgB_2 via ball milling methods, producing $MgBH_4$ in the process. Fujii[13] conducted the first attempt to hydrogenate elemental boron powder, also using ball milling. Their results suggest that 2.3 wt% hydrogen loading was achieved after 80 h of milling under 10 atm of H_2.[13] There is some precedence for use of hydrogenation to improve

ignitability of diesel fuel,[14] and the effects of hydrogen loading on conventional hydrocarbon fuels such as gasoline,[15] jet fuel[16] and natural gas[11,17,18] has also been studied. Results suggest that thermal efficiency was increased and fuel consumption was reduced when the optimum proportion of hydrogen is added. Furthermore, evidence of reduced CO emission was also observed for hydrogen enriched fuels.[11,16,19]

Here, ball milling was used to prepare boron nanoparticles and load them with up to 5 wt% hydrogen – comparable to the DOE target for hydrogen storage systems (5.5 wt% by 2017).[20] We show that the hydrogen remains incorporated into the boron samples when the H_2 pressure is removed, and use a variety of theoretical, spectroscopic, and mass spectrometric methods to probe how the hydrogen is bound, and the energies required to release it. The effects of air exposure are also probed, showing that the hydrogen-loaded boron does, indeed, oxidize more readily than boron prepared under inert atmosphere. The effect of hydrogenated boron loading on the hypergolic ignition of two ionic liquids was also tested, using white fuming nitric acid as the oxidizer.

Results and Discussion

Quantifying hydrogen loading in boron. Hydrogen uptake was monitored throughout the milling process by measuring the pressure drop inside the milling jar at intervals, until the pressure stabilized after ~15 hours of milling, indicating that H_2 had essentially saturated the particles. **Figure 1a** shows the pressure drop inside the milling jar for three sets of conditions. Data are shown for milling of 2 grams of boron and 160 grams of tungsten carbide media in 60 psia (4 atm) initial H_2 pressure. For comparison, analogous pressure versus time data are given for identical milling runs where either the boron was omitted, or the jar was filled with argon instead of H_2. For the run with H_2 and boron, the absolute pressure dropped by nearly a factor of

three over the 15 hour milling run. In contrast, there was no significant pressure drop for the run with boron in argon, showing that boron does not absorb argon significantly. The jar pressure was also constant for the run with H_2 but no boron, showing that that the jar seal is not permeable to H_2, and that the tungsten carbide media and jar lining do not take up any significant amount of hydrogen.

Several different experiments were carried out varying the initial boron feedstock mass and H_2 charge pressure, and the results were summarized in **Figure 1b**, where the H_2 pressure drops have been converted to the equivalent H_2 uptake, expressed as H_2 consumed as a weight percent (wt%) of the initial boron mass in each experiment. The H_2 weight percent consumed varied from ~3 wt% to 5 wt%, increasing with increasing ratio of H_2 to boron in the initial jar loading. We have not attempted milling at higher H_2 pressures due to limitations of the jar seal design, however, we note that the H_2 uptakes observed here are higher than the 2 – 3 wt% hydrogen loadings observed in previous studies that used higher H_2 pressures and much longer milling times (70 − 145 psi, 80 − 100 h).[13,21] To see if higher loadings could be obtained if the H_2 pressure was not allowed to drop as hydrogen was taken up by the sample, we also tried experiments where the H_2 was periodically added to the jar to bring the pressure back to 60 psia, and where the milling was extended to 24 hours, but this did not result in any additional loading.

An obvious question is whether the hydrogen taken up by the boron during milling remains in the sample when the H_2 overpressure is removed. Therefore, we also directly measured the hydrogen content of one of the milled samples using TC/EA, as described above. For this analysis the sample used was one where the H_2 loading calculated from the pressure drop during milling was 3.4 wt%. TC/EA analysis found evolution of 3.5 wt% of H_2 when the sample was heated to 1400 °C. It is important to note, however, that the TC/EA instrument is

not equipped with an inert sample transfer system, thus the sample was exposed to air. Air exposure might result in some hydrogen loss from the boron due to oxidation of the boron particle surface, but might also lead to uptake of hydrogen in the form of atmospheric water or other hydrogen-containing contaminants. Therefore, a sample of the unmilled boron feedstock was also analyzed by TC/EA, resulting in a measured hydrogen content of ~0.4 wt%. The TC/EA analysis shows, therefore, that milling boron in H_2 increased the hydrogen content by at least ~3.1 wt%. The extra hydrogen content is slightly lower than the 3.4 wt% uptake inferred from the pressure drop during milling, however, lack of quantitative agreement is not surprising given the possible effects of air exposure prior to TC/EA analysis. We tentatively conclude, therefore, that the H_2 pressure drop really does reflect some process by which H_2 is taken up by the boron under milling conditions, binding in such a way that it is not lost under ambient conditions.

DFT results on possible modes of hydrogen uptake by boron. Before discussing experiments designed to probe the nature of the hydrogen binding in the H_2-loaded samples, we first briefly outline several possibilities, and present theoretical results on different binding geometries. The first point to consider is the magnitude of the hydrogen uptake, which ranges up to 5 wt% – close to the 5.5 wt% hydrogen storage target set by DOE for 2017 on-vehicle storage. Given the atomic weights of H (1.008 g/mole) and B (10.81 g/mole), 5 wt% corresponds to ~36 mole %, or a stoichiometry of 1 H atom for every ~1.8 B atoms. There are several mechanisms that could result in such high hydrogen uptakes. Note that milling of brittle materials, like boron, essentially involves crushing boron particles between the tungsten carbide milling media and jar, exposing fresh boron surfaces.

One possibility is that H_2 reacts with these fracture surfaces, for example, by dissociating and forming B−H bonds reminiscent of those found in borane compounds. If we assume that B−H bond formation occurs only on the surfaces of the particles, and that every surface B atom has a single H atom bound to it, then this scenario would require that ~56 % of the B atoms be in the surface layer – corresponding to 1200 m^2 of available surface binding sites per gram of boron, assuming that the density of milled product is equal to that of the amorphous boron feedstock (2.37 g/cm^3). As discussed in the supporting information (**Figure S1**), if spherical, such particles would have an average diameter of ~2 nm.

Alternatively, some hydrogen might be taken up by interstitial sites in the boron particle bulk, and in that case, such high particle surface area would not be required to account for the high hydrogen loading. Several of the isomorphs of crystalline boron are built of hollow B_{12} icosahedra, and it is known that amorphous boron also includes randomly oriented B_{12} icosahedra.[22] The presence of such structures raises the possibility that either atomic or molecular hydrogen might bind to, or become physically trapped in the interior of the icosahedra. It is not clear what the signature of such interior hydrogen would be experimentally.

Another final possibility is that hydrogen might react with boron under milling conditions to generate stable borane molecules. For example, if we assume that the H_2 reacts with boron to produce diborane gas (B_2H_6), the result would be a pressure drop of a factor of three (at 100 % conversion), in reasonable agreement with our observation (**Figure 1a**). Formation of higher molecular weight boranes such as tetraborane ($B_4H_{10(g)}$) pentaborane ($B_5H_{9(\ell)}$) or decaborane ($B_{10}H_{14(s)}$) would result in larger pressure drops, for a given extent of conversion. Most of these species have significant vapor pressures, and therefore should be observable by mass spectrometry of the milling jar headspace, or of gases evolved when samples are heated, as

described below. To the extent that such boranes are volatile, they would tend to be lost during transfer of samples to analytical tools such as the TC/EA instrument used to verify the hydrogen loading, as discussed above.

Density functional theory (DFT) calculations were conducted to assess the stability of various boron-hydrogen bonding arrangements, and the activation energies for their formation. The boron particle was represented by a B_{80} cluster which contains both a variety of different boron surface sites, as well as bulk-like interstitial sites, as discussed in the Supporting Information (**Figure S2** and accompanying discussion). We first examined the interaction of a single H_2 molecule with various sites on the surface of B_{80}. Typical optimized structures and reaction coordinates are shown in **Figures 2 and S3 – S10**. Dissociative adsorption of hydrogen to form borane-like B−H bonds on adjacent B atoms is energetically favorable, with activation barriers in the 5 – 33 kcal/mol range, depending on which part of the B_{80} cluster is involved **(Figures 2 and S3)**. As shown in these figures, the dissociative reaction pathways involve initial weak (<1 kcal/mol) long range interaction of H_2 with the cluster, and then initial attack of H_2 on a single B atom, forming a transition state. The arrows shown on the transition state structures are the motions corresponding to the single imaginary frequency at the transition state, i.e., the reaction coordinate. As the H_2 dissociates to form B−H bonds on adjacent boron atoms, the B−B distance between these atoms also increases effectively breaking the B−B bond.

For milling conditions, where the temperature approaches 100 °C, such reactions should be facile. A molecularly bound H_2-B_{80} complex was also observed (**Figure S4**), however, it is predicted to be energetically unfavorable and would dissociate back to H_2 + B_{80} at non-zero temperatures. Once an adsorbed H_2B_{80} complex is formed, the H atoms can migrate on the B_{80} surface, with activation barriers in the 1 to 22 kcal/mol range, depending on which sites are

involved (**Figures S5 - S8**). Complexes where one of the H atoms is bridge-bonded to a pair of B atoms were also observed (**Figure S9**), but these are higher in energy than complexes with both H atoms in terminal B-H bonds, and the activation barrier stabilizing the bridge-bonded structure is low (~3 kcal/mol), suggesting that bridge bonded structures should be kinetically unstable. **Figure S10** summarizes the structures of different H_2B_{80} isomorphs (with H_2 dissociatively adsorbed) investigated, which were found to be stable with respect to $H_2 + B_{80}$ reactants by between 3.5 and 60 kcal/mol.

The possibility of hydrogen binding into interstitial sites was also considered in these calculations. For $H_2@B_{80}$, i.e., B_{80} containing a single H_2 molecule trapped interstitially (**Figure S11**), the energy is found to be 62.7 kcal/mol above the $H_2 + B_{80}$ reactants, however, if zero point energy is included, then this structure is unstable with respect to dissociation of the interstitial H_2 to two interstitial H atoms. This structure with two interstitial H atoms is still 56.3 kcal/mol above $H_2 + B_{80}$, i.e., far above the energies of structures with both H atoms bound on the B_{80} exterior. We also examined the energetics for migration of one of the exterior H atoms in H_2B_{80} migrating to an interstitial site, and found that the process is unfavorable by 57 kcal/mol, with a barrier of 58.4 kcal/mol. It seems clear, therefore, that when H_2 attacks a clean boron surface, dissociative adsorption with both H atoms remaining on the surface, is far more energetically favorable than interstitial trapping of either H, H_2, or 2 H. The possibility remains, however, that H or H_2 might trap in interstitial sites after all the surface sites are saturated.

The process of saturating the B_{80} surface was probed via DFT calculations on H_xB_{80} (x = 56, 58 and 60). The total energies with respect to $^x/_2$ $H_2 + B_{80}$ are as follows:

$28H_2 + B_{80} \rightarrow H_{56}B_{80}$ $\Delta Hr = -681$ kcal/mol;

$29H_2 + B_{80} \rightarrow H_{58}B_{80}$ $\Delta Hr = -710$ kcal/mol

$30H_2 + B_{80} \rightarrow H_{60}B_{80}$ $\Delta Hr = -644$ kcal/mol.

Optimized structures for $H_{58}B_{80}$ and $H_{60}B_{80}$ are shown in **Figures S12 and S13.** From the total energies above, we can calculate that the H_2 addition reaction $H_2 + H_{56}B_{80} \rightarrow H_{58}B_{80}$ is exoergic by 29 kcal/mol, whereas the subsequent addition $H_2 + H_{58}B_{80} \rightarrow H_{60}B_{80}$ is endoergic by 66 kcal/mol, i.e., $H_{58}B_{80}$ represents saturation of the surface. The structure for $H_{60}B_{80}$ shown in **Figure S13** suggests that while bridging (B−H−B) bonds become more likely in saturated structures, terminal B−H bonding still predominates.

To examine the possibility of binding hydrogen interstitially after saturating the surface, the energy was calculated for $H@H_{57}B_{80}$, i.e., for $H_{58}B_{80}$ where one of the surface H atoms was moved into an interstitial sites. We were unable to find a transition state for this process, but it is clear that moving an H atom from a surface site to an interstitial site is ~36 kcal/mol endoergic. Finally, to test the energetics for trapping H_2 inside boron where the surface is already saturated with B−H bonds, energetics were calculated for $H_2@H_{58}B_{80}$ and $H_2@H_{60}B_{80}$ (**Figures S14 and S15**). The energy for $H_2@H_{58}B_{80}$ is 74.2 kcal/mol above $H_2 + H_{58}B_{80}$, however, if zero point energy is included, then the barrier for dissociation of the interstitial H_2 vanishes, and one of the resulting H atoms emerges to the surface, generating $H@H_{59}B_{80}$, with an energy 28 kcal/mol above $H_2 + H_{58}B_{80}$. The energy for $H_2@H_{60}B_{80}$ is 35 kcal/mol above $H_2 + H_{60}B_{80}$, but note that $H_{60}B_{80}$ is already metastable by 66 kcal/mol with respect to $H_2 + H_{58}B_{80}$.

In summary, the theory clearly shows that surface B−H binding, up to a saturation level approaching one H atom per surface boron atom, is energetically favorable, with activation energies in a range that should allow facile reaction at the <100 °C temperatures range of the mill. Interstitial binding is far less energetically favorable, and interstitial hydrogen is metastable with respect to migration to surface sites. The theory, therefore, predicts that interstitial

hydrogen binding in boron should be insignificant, at least via interaction of H_2 with boron surfaces.

IR and XPS spectroscopy. Infrared spectroscopy provides a probe of B−H bonding in the milled samples, and an example spectrum is shown in **Figure 3**. Unfortunately, the FTIR instrument was not equipped for inert sample introduction, and therefore this sample was exposed to air prior to analysis. The boron oxidation state in air-exposed samples was probed by X-ray photoelectron spectroscopy (XPS), as shown in **Figure 4**. Most of the B 1s XPS signal comes from the top ~6 nanometers of the boron surface (see Supporting Information), thus the appearance of a substantial peak for B^{3+} at 193 eV is consistent with the sample having a thin oxidized surface layer passivating the unoxidized core of the particles, which gives rise to the large peak for B^0 at 188 eV. The B 1s binding energy for B^{3+} in materials such as B_2O_3, $B(OH)_3$ and various borates is quite similar,[23] thus XPS provides no information on the hydration state of the oxidized layer.

Consistent with the XPS result showing surface oxidation, the infrared spectrum (**Figure 3**) of the H_2-loaded boron is dominated by strong bands assigned to B−O stretching (1434 cm^{-1}) and O−H stretching (3202 cm^{-1}) vibrations.[24] The strength of the O−H stretch band suggests a significant degree of hydroxylation, i.e., the surface oxide layer appears to be partially hydrated. The IR spectrum also shows a strong peak at 2507 cm^{-1} which is in the range typically seen for B−H stretching vibrations in borane compounds,[25] confirming that at least some of the hydrogen is in the form of H atoms covalently bound to boron. The B−H stretch frequency for H atoms bound to B atoms on the surface of solid boron is not known, but might be expected to be similar to B−H stretches in boranes. The IR spectrum, therefore, does not rule out formation of boranes as the mechanism for hydrogen uptake under milling conditions, although to survive transfer in

air to the FTIR instrument, such boranes would have to be both non-volatile and air-stable, ruling out any of the low molecular weight boranes.[26] Further evidence on the borane issue is presented below.

The DFT theory provides additional information for interpretation of the IR spectra. Example results are shown in **Figures S16-S18**, which show the calculated IR spectra for several B_{80} clusters with both external and interstitial H atoms. Figure S16 shows the spectrum of $H@HB_{80}$, i.e., a cluster with one interstitial and one external H atom. There is a dense band of weak transitions between ~200 cm^{-1} and ~1300 cm^{-1} corresponding to modes of the B_{80} cage, and this band is similar in all the calculated structures. There are two bands at 1416 cm^{-1} and 2045 cm^{-1} corresponding to asymmetric and symmetric stretching modes of the bridge-bonded interstitial H, and a prominent peak at ~2627 cm^{-1} which is the stretch of the external B-H bond. The experimental materials have much higher hydrogen content, thus the spectra for $H@H_{59}B_{80}$ and $H@H_{57}B_{80}$ are more relevant. Both show the dense band between ~200 cm^{-1} and ~1300 cm^{-1} corresponding mostly to modes of the B_{80} cage. The boron skeletal modes are shifted to lower frequency compared to those for $H@HB_{80}$, showing the overall weakening of the B-B skeletal bonds in the hydrogen-saturated cluster. Modes associated with terminal B-H stretching from a band between ~2550 cm^{-1} and 2700 cm^{-1}, and modes associated with stretches of H atoms in bridging sites lie in the 2000-2300 cm^{-1} range. In addition, there are peaks between ~1400 cm^{-1} and 2200 cm^{-1} corresponding to various mixed bending+stretching motions of the hydrogen atoms, and between 1000 cm^{-1} and 1200 cm^{-1} there are modes which combine hydrogen bending with boron skeletal distortions. For both clusters, the modes associated with the interstitial H atoms are indicated, and found to have frequencies in the same general range as those for the external H atoms.

The experimental spectrum shows a band for B−H stretching peaking at 2507 cm^{-1}, which is narrower that might be expected from the theoretical spectrum, however, this probably reflects the fact that there is considerable site-to-site variation in the stability of hydrogen chemisorption on the B_{80} cluster (**Figure S10**), which presumably is reflected in the broad range of B-H stretching frequencies. Apparently the small boron nanoparticles produced experimentally, are more homogeneous from the perspective of B−H binding. The hydrogen "bending" band calculated to lie between ~1400 cm^{-1} and 2200 cm^{-1} presumably would also be narrower in the experimental spectrum, and may give rise to the unassigned peak near 1600 cm^{-1}, but could also be obscured by the BO stretch band of the oxidized surface. The boron cage modes are calculated to give rise to a weak band between ~200 cm^{-1} and ~1300 cm^{-1}, which is not obvious in the experimental spectrum, possibly because it is simply too weak. It is also likely that in nanoparticles, this band may shift to lower frequencies, and in that case it would be out of the experimental range.

Comparison with boron milled under other conditions. As shown in **Figure 4**, the relative intensity of the B^{3+} peak in the B 1s XPS of boron that was dry-milled in H_2 and subsequently exposed to air, is ~5 times greater than that observed for boron dry-milled in argon (or N_2 atmosphere) prior to air exposure. This observation indicates that the concentration of oxidized boron in the surface region of the air-exposed samples is significantly higher for the H_2-milled sample. For bulk boron, air exposure results in formation of a self-limiting oxide layer ~0.4 nm thick,[6] while XPS samples the top ~6 nm of the sample (see Supporting Information). The greater extent of boron oxidation for the H_2-milled sample could indicate that hydrogen loading increases thickness of the self-limiting oxide layer, perhaps by increasing the permeability of the initial oxide layer to O_2. Greater oxidation would also be explained,

however, if H_2-milling changed the morphology or size distribution of the resulting particles. If, for example, the H_2-milled boron contained a larger fraction of particles in the few nanometer diameter range, the ratio of oxide layer to unoxidized core would be large, and XPS would "see through" the particles and detect a large oxide concentration. Similarly, if the H_2-milled particles were rougher, with nanometer scale asperities, then a larger fraction of the XPS-detectable surface region would oxidize on air exposure. Either scenario would also help account for the very high surface area/gram required to account for the high hydrogen uptake observed in H_2-milled boron.

The size distribution obtained in milling is determined by the balance between size reduction by crushing of particles, and particle growth by cold welding, which can occur when particles are forced together by impacts. Generally, size reduction is more efficient when wetting agents are used to help keep particles well dispersed, and to reduce cold welding.[6] In fact, similarly high signal for B^{3+} is also seen in XPS of boron milled under Ar or N_2, but with hexane added as a non-reactive wetting agent.[6] The interesting question, therefore, is whether gaseous H_2 is also somehow acting as a milling agent, improving the size reduction process either by increasing the tendency for particles to fracture on impact, or by reducing cold welding via formation of a B−H surface layer.

Figure 5 compares SEM images of boron nanoparticles obtained by dry milling in H_2 and Ar atmospheres. The Ar-milled nanoparticles actually appear smaller than the H_2-milled particles, however, they also have noticeably more compact, almost spherical structures, whereas the H_2-milled particles are highly irregular, with a broader size distribution, including a larger population of the smallest size particles. The highly irregular structure of the larger particles is likely a sign that these are actually aggregates of smaller, primary particles, and if the internal

surfaces of these aggregates are accessible to H_2 and O_2, this would account both for the high hydrogen update, and the observation of a greater extent of oxidation upon air exposure.

Boron, because it is a low Z element, is difficult to study in TEM, but **Figure 5** also shows a TEM image of one of the small particles generated by H_2-milling. Electron energy loss spectroscopy was used to verify that the particle was boron. The fact that the contrast is relatively constant across most of this particle, suggests that it has a flat, plate-like structure. More spherical particles would be thinner, with lower contrast, near the edges than in the middle. The areas of higher contrast to the upper left and upper right of the particle indicate thicker regions, which are tentatively ascribed to smaller particles binding to the main particle, such that the aggregate thickness is higher. Plate-like primary particles would tend to have high surface area/volume ratio, again consistent with high hydrogen uptake, and oxidation upon air exposure.

Mass Spectrometry of Headspace and Desorbing Gases. As noted, both the hydrogen uptake and the appearance of B−H bonds in the IR spectrum could result either from H atoms chemisorbed on the boron particle surface, or from formation of boranes that are simply mixed with boron particles in the sample. Mass spectrometry was, therefore, used to look for the signature of boranes in the milling jar headspace gas, and also in gases evolved from the boron samples during heating. To avoid loss or destruction of low molecular weight boranes, which are volatile and reactive, the mass spectrometry experiments summarized in **Figures 6** and **7** were done carefully avoiding air exposure. **Figure 6** shows a typical mass spectrum of the headspace gas collected from the jar after milling in H_2. For this experiment, argon was added to the initial gas mixture at a 12:1 H_2:Ar ratio, in order to have a known concentration of Ar in the headspace as an intensity standard. As expected, the headspace spectrum included prominent peaks from

H_2 (m/q = 2, 1) and Ar (m/q = 40), as well as numerous small peaks attributed to organic ions, resulting from organic contaminants in the boron feedstock (see below).

There are two interesting features of the spectrum. There is a set of small peaks (m/q = 18, 17, 16) indicating the presence of water. Some water is expected because the 95 % pure boron feedstock is known to contain water, and there is also oxygen present on the feedstock particle surfaces that might react with H_2 to form water under milling conditions. Evolution of water and isotope labeling experiments are discussed below.

More importantly, the mass spectrum provides no evidence for the presence of volatile boranes. Such boranes all have characteristic patterns of peaks corresponding to stable $B_xH_y^+$ stoichiometries, and reflecting the 5:1 ^{11}B:^{10}B natural abundance.[25] For example, under electron impact conditions similar to ours, standard mass spectra of stable B_nH_m ($n \leq 6$) compounds all show substantial peaks at m/q = 11, which is absent in our spectrum. Furthermore, the borane spectra include families of $B_xH_y^+$ peaks that lie in m/q ranges (23 − 27, 33 − 38, 44 − 50) where there is essentially no signal in our spectra. We conclude, therefore, that the B−H covalent bonds observed in the IR spectrum, and the high hydrogen uptake, do not result from formation of low molecular weight boranes. This conclusion is consistent with the TC/EA and IR experiments, where volatiles would have been lost during sample transfer, which showed substantial retention of hydrogen content, and the presence of B-H bonds in the samples.

Mass spectrometry was also used to monitor gases evolved from the particles as they were heated to 350 °C, to see if any higher molecular weight borane species might be present. To help distinguish between hydrogen introduced by milling and hydrogen present as feedstock contaminants such as water and hydrocarbons, the gas evolution experiments were performed using boron milled in a D_2 atmosphere. The first point of interest is that uptake of D_2 by boron

appears to be essentially identical to that of H_2, as determined from pressure decreases during milling. The similarity indicates that there are no significant deuterium isotope effects on the uptake process, or on H vs. D binding to the boron. After preparation of the deuterium-loaded sample, the jar was opened in the glovebox, and a sample of the boron powder was placed into a glass tube, thus allowing volatiles such as D_2 to escape. Volatile boranes would also have been lost, however, the results in Figure 6 show that none are produced in the hydrogen-milling process. The sample tube was valved closed in the glovebox, then connected to the mass spectrometer inlet system, which was evacuated to avoid air exposure, prior to opening the valve to allow gas sampling.

Figure 7 shows the results. At the bottom, two spectra are given showing typical instrument baseline data. The bottom spectrum, taken at the beginning of the day, shows significant signals only for hydrogen (m/q = 2), water (m/q = 18, 17, 16), CO/N_2 (m/q = 28), and CO_2 (m/q = 44). The second baseline spectrum was taken just before the start of the heating series, with elevated water signal (m/q = 18, 17, 16) as a result of water introduction during experiments done earlier in the day. The spectrum labeled 25 °C shows the gases from the sample container before heating was started, and the only significant new signal, compared to the pre-heating baseline, is from glovebox nitrogen (m/q = 28, 14) trapped in the sample container. There is no evidence of H_2, HD, or D_2 evolving from the sample at room temperature.

The sample was then heated to 350 °C, slowly enough (5 hours) to insure that the temperature throughout the powdered sample was reasonably homogeneous. During this slow heat ramp, the gases evolved from the sample were continuously leaked into the mass spectrometer gas inlet, with mass spectra recorded at selected temperatures. Therefore the spectra represent snapshots of the gases evolving at particular temperatures during the heat ramp.

By the time the 120 °C spectrum was recorded (~30 minutes), the glovebox N_2 had largely been pumped out, as shown by negligible m/q = 28 signal. In addition, the water signals also decreased by ~60 % relative to the pre-heating baseline, reflecting a combination of loss of water from the sample, and slow recovery of the instrument baseline water signal. More importantly, the spectrum shows small signals for HD, and D_2 evolving from the sample. Interestingly, there is no evidence for D_2O or HDO evolution at either 25 °C or 120 °C, where desorption of molecularly adsorbed water might be expected. This absence indicates that molecularly adsorbed water is not formed by reaction of the D_2 milling atmosphere with oxides or hydroxides initially present on the surface of the boron feedstock. Furthermore, we can infer that H_2O, known to be present as a contaminant in the feedstock, does not undergo exchange with D bound to the boron.

As the temperature is increased, the signals for H_2, HD, and D_2 increase significantly, dominating the mass spectra. The large H_2 signal is attributed to significant hydrogen contamination of the feedstock. HD signal indicates that isotope scrambling is reasonably efficient, which is consistent with the theoretical prediction that hydrogen is dissociatively chemisorbed to the boron surfaces, so that desorbing hydrogen is produced by recombination of H and D. At higher temperatures, small peaks at m/q = 19 and 20 were observed, indicating desorption of a small amount of water produced by recombination of dissociated species such as H and OH (and isotopologs), thus allowing isotope scrambling. With increasing temperature, a number of small peaks appear in the mass ranges 12 – 15, 24 − 32 and 40 – 46. As shown in **Figure S19**, these clearly originate from organic contaminants in the boron feedstock, which can be removed, if necessary, by prolonged vacuum outgassing (**Figure S20**).

The results in **Figure 7** show no signs of boranes evolving from the sample in the temperature range up to 350 °C. The m/q = 11 signal seen for all boranes[25] is not observed, for example. The fragment ion patterns for deuterated boranes have not been reported to our knowledge, but would be broadened and shifted to higher mass, compared to the known spectra[25] for boranes. For example, the prominent $B_3H_x^+$ (x = 0 – 5) peaks seen for tetraborane and pentaborane would appear in the range m/q = 33 to 43, and while there are some small peaks in this mass range, the intensity pattern is not consistent with $B_3D_xH_y^+$ ions, and suggests, instead, that the origin is fragment ions from the hydrocarbon contaminants.

Thermogravimetric analysis with mass spectrometry (TGA-MS). To probe mass loss quantitatively, and to examine gas evolution over a wider temperature range, samples prepared by milling in D_2 atmosphere were characterized with TGA-MS, and the results are given in **Figure 8**. It is important to note that these samples were never exposed to air, and TGA was done inside a nitrogen glovebox, therefore, any hydrogen- or oxygen-containing species observed in the analysis originate from the sample. The instrument use has, however, several limitations. It was only possible to monitor a small set of ion masses during the TGA heat ramp, which were chosen as H_2^+, D_2^+, H_2O^+, D_2O^+, B^+ and $B_2D_5^+$. The latter two masses would be indicative of signal from deuterated boranes, and have little or no contribution from cracking of hydrocarbon ions. In addition, the mass spectral sensitivity of the TGA-MS instrument was found to be a strong function of mass. In particular, the sensitivity decreased rapidly at low m/q, affecting our ability to monitor H_2 and D_2 evolution. No signal was observed for H_2^+, even though the mass spectra in **Figure 7**, where sensitivity was calibrated, show this to be a major product ion. The signal for D_2^+ was sufficient to allow TGA-MS measurements, but comparison

with **Figure 7** indicates that the D_2^+ sensitivity is at least 25 times lower than that for H_2O^+, which was the most intense mass spectral signal observed.

The top frame of **Figure 8** shows the percent mass change versus temperature, and the raw ion intensities for D_2^+, D_2O^+, and H_2O^+ are shown in the bottom frame. A rapid ~1.5 % mass loss was observed between ~100 °C and 150 °C, and the mass spectral results suggest that ~1 % corresponds to desorption of undeuterated water attributed to water in the boron feedstock. A somewhat slower mass loss continued as the sample was heated up to 900 °C, totaling ~6 %, i.e., ~5 % mass loss if the contribution from water is subtracted. The pressure drop during production of this sample was consistent with ~6 wt% deuterium loading, thus the mass loss, not including water, was about 1 % less than expected. This may simply indicate that higher temperatures would be required to lose all the deuterium. The mass spectral results (**Figure 7**) indicate that the primary loss was of D_2, HD, and H_2, although only D_2 could be monitored in the TGA-MS. The D_2 desorption temperature dependence shows evidence of two broad features, peaking at ~270 °C and ~480 °C. These have previously been attributed to recombinative desorption from sites with terminal B−D and bridging B−D−B bonds, respectively,[13] although the FTIR results above show no evidence for bridge-bonded hydrogen, and the theory also suggests that terminal bonding is both more important and more stable. Clearly, the hydrogen loaded into boron by milling is strongly bonded, with temperatures approaching 900 °C required to desorb it. The high desorption temperature would clearly be problematic for hydrogen storage applications, however, for applications to propellants or fuels, the strong B−H binding is advantageous, insuring that the hydrogen is not lost during storage. Under combustion conditions, the hydrogen would be consumed as the boron burned, resulting in an increase in I_{sp} due to additional low molecular weight products. There is also the possibility that presence of

hydrogen on the boron surface might significantly enhance ignition, because, by analogy with boranes, the B−H bonds are likely to be reactive with oxidizers.

The D_2O intensity trace is also interesting. During the strong initial pulse of water desorption around 120 °C, there is little if any D_2O desorption, however, there are also weak water desorption features between ~250 °C and 400 °C, and both H_2O and D_2O are observed in these. These TGA-MS results are consistent with the conclusion reached above, that milling in D_2 does not result in significant production of molecularly adsorbed deuterated water, thus the water signal around 120 °C, corresponding to desorption of this molecularly adsorbed water, shows no isotope exchange. The higher temperature desorption features correspond to recombinative desorption, where H/D scrambling is facile. This two stage water desorption behavior is somewhat reminiscent of water desorption from boric acid (H_3BO_3).[27]

Reactivity with oxygen. Reactivity of hydrogenated boron nanoparticles with oxygen was investigated by monitoring mass gain as samples were heated under an O_2 gas flow using a TGA system. **Figure 9** compares results for samples of hydrogen-milled and argon-milled boron. For Ar-milled boron, the sample mass was essentially constant up to about 100 °C, and then there was a slow increase totaling ~1 % as the temperature was ramped up to ~400 °C. At that point, the rate of mass gain increased, reaching a maximum at 500 °C, before tapering off above ~550 °C. For this sample, which was transferred to the TGA in air, the boron particles were coated and passivated by a thin oxide layer, as shown by the XPS results in **Figure 4.** For temperatures well below the B_2O_3 melting temperature (450 °C), slow mass gain is expected because diffusion of oxygen through the passivating oxide layer is slow. As the oxide approaches and passes its melting point, oxygen diffusion becomes fast, and the oxide layer grows at an increasing rate, with concomitant increase in mass. The temperature range probed is

well below the oxide sublimation temperature (1500°C) thus the oxidation products remain on the particle surface, thickening the oxide layer, and leading to eventual slowing of the mass gain rate.

The H_2-milled sample used in this experiment had ~3.5 wt% of hydrogen uptake. The XPS data in **Figure 4** shows that when such H_2-milled samples are exposed to air during sample transfer, the fraction of oxidized boron in the surface region is substantially greater than in the Ar-milled sample. This increased oxidation could indicate that incorporated hydrogen increases reactivity toward oxygen, but also could reflect increased surface area (**Figure 5**). When hydrogenated boron oxidizes in air, it could form B_2O_3 (as in unhydrogenated boron), but one might expect that the surface would consist of hydrated forms of the oxide, such as $B(OH)_3$, HBO_2, or $H_2B_4O_7$, which form in oxidation of boranes.[28,29] The presence of some degree of hydration is confirmed by the strong OH stretching signal observed in the IR spectrum of oxidized, H_2-milled boron (**Figure 3**).

As such a sample is heated, the surface layer would tend to dehydrate, leading to an initial mass loss, and just such an initial mass loss of 3 % is observed as the sample was heated to 100 °C. Note, however, that the mass loss stops well below the temperature expected for complete dehydration to B_2O_3 (250 °C for bulk boron oxide), and mass begins to increase again above 100 °C. Furthermore, the rate of mass gain in the 100 °C to ~420 °C temperature range is five times faster than the rate observed for the Ar-milled sample. Faster oxidation of the H_2-milled boron is attributed to some combination of higher reactivity of the hydrogen-loaded boron, and higher surface area. For the H_2-milled sample, the transition to rapid mass gain occurs at ~420 °C, compared to ~500 °C for Ar-milled boron, and in addition, the transition is more abrupt and the subsequent rate of mass gain is faster than for the Ar-milled sample. All

three of these factors suggest that the changes in surface properties resulting from H_2 milling, should lead to more facile ignition of H_2-milled boron under combustion conditions.

Effects of hydrogenation on performance as a fuel additive. The specific impulse, I_{sp}, is a measure of the amount of thrust obtainable in rocket propulsion, from a given mass of fuel. I_{sp} is proportional to the exhaust velocity, and therefore depends on the distribution of molecular weights of the combustion products as well as the exhaust temperature. Hydrogen addition tends to generate lower molecular weight products, and should improve I_{sp}. To estimate the potential impact of hydrogen loading, the I_{sp} of hydrogenated boron was calculated using the U.S. Air Force I_{sp} computational model.[30] Specific impulse values were calculated for the system at standard conditions; that is, chamber pressure was set at 1000 psi, engine exhaust was set to sea level pressure through an optimized nozzle expansion.[31] The heat of formation and physical property input data for oxidizer and fuels for the calculations were from the literature.[32,33] The physical model of the hydrogenated boron particles assumes hydrogen is taken up through covalent bonds to boron atoms to form a borane-like shell (modeled as decaborane) over an elemental boron core. For hydrogenated boron particles with 5 wt% hydrogen content, the core/shell ratio is 56.7:43.3.

The theoretical I_{sp} was calculated to be 276 s for a bipropellant baseline system consisting of a kerosene-based fuel (RP1) and the liquid storable oxidizer, dinitrogen tetroxide (NTO). In comparison, theoretical performance of a bipropellant system incorporating 10 % concentration of 5 wt% hydrogenated boron in the RP1 fuel is 280 s. An additional calculation was conducted with fully hydrogenated particles (essentially decaborane) and for the same 10% concentration, a specific impulse of 284.5 s was obtained. Thus, as the degree of hydrogenation of the particles increases, there is some increase in I_{sp}, as expected, however the effect is not dramatic. As

pointed out above, however, there is also the possibility that hydrogenating the boron, to create a borane-like surface, might substantially increase the reactivity toward oxidizers, and therefore improve the ignition and combustion properties of the fuel. Some suggestion of this effect is observed in **Figure 9**, where oxidation begins at lower temperature and is more rapid, than for Ar-milled boron.

As a first test of this possibility, we examined the effects of small loadings of hydrogenated boron on the hypergolic ignition of two ionic liquids, using methods we have previously reported.[34] 1-butyl-3-methyl-imidazolium dicyanamide ([BMIM][DCA]) and 1-methyl-4-amino-1,2,4-triazolium dicyanamide ([MAT][DCA]), were added under an Ar atmosphere in a glovebox to pre-weighed flasks containing both H_2-milled (B-H_2) and D_2-milled (B-D_2) boron nanoparticles. The sealed 0.3 wt% mixtures were placed in a Branson 5510 bath ultrasonicator for four consecutive 99-minute cycles until no nanoparticles were visible at the bottom of the vial. The resulting suspensions appeared slightly opaque relative to the clear, slightly yellow color of the neat ILs. The suspended B-H_2 and B-D_2 nanoparticles began settling out after ca. 24 h from [BMIM][DCA] and after ca. 36 h from [MAT][DCA] with no difference in suspension stability whether the boron particles were milled under H_2 or D_2. Once settling was observed, samples could be redispersed, through the same process. The enhanced suspension stability for [MAT][DCA] vs. [BMIM][DCA] was also observed for boron nanoparticles milled in, and capped with [MAT][DCA], as previously reported.[34]

It is interesting to note that the boron samples milled under H_2 were not only less stable in these ILs than boron nanoparticles milled in the presence of [MAT][DCA] without H_2,[34] but that resuspending the B-H_2 nanoparticles required full repetition of the 4 x 99 min cycles of sonication. Boron nanoparticles milled in [MAT][DCA] stayed suspended longer and required

only simple vortex mixing after settling. The difference is attributed to differences in the surface chemistry of the particles. Particles milled in [MAT][DCA] (or [BMIM][DCA]) are capped with a layer of the IL that is bound strongly enough to resist vigorous solvent washing, and to protect the particle surface from air oxidation. Zeta potential measurements show that the particles are charged by binding of MAT^+ in the case of [MAT][DCA], and of DCA^- in the case of [BMIM][DCA].[8] As shown above, the hydrogen-milled particles are simply capped with a layer of covalently bound H atoms, and the H-capped particles are obviously less IL-compatible than the charged, IL-capped boron.

While suspended, the B-H_2 nanoparticle-loaded ILs were tested for hypergolic ignition. A 10 μL aliquot of the IL fuel was dropped *via* Hamilton syringe into a vial containing 500 μL of white fuming nitric acid (WFNA) oxidizer[35,34] and the resulting ignition was monitored with a high speed camera (**Figures S21 – S24**). Upon contact with the WFNA, the neat samples of [BMIM][DCA] and [MAT][DCA] resulted in a single ignition with an ignition delay of 41 and 34 ms, respectively (**Table 1**). Samples tested with 0.3 wt% B-H_2 loading had ignition delays that were identical to those for the neat ILs, within the measurement uncertainties, however, there were changes in the ignition and combustion characteristics, as discussed below.

B-H_2 in [BMIM][DCA] led to more vigorous combustion, as shown by a slightly improved flame height (from 4 cm to 5 cm), a much longer overall flame duration, and the observation of multiple flames. Both the insensitivity of ignition delay to the presence of a small particle loading, and the observations of altered flame characteristics, closely match our previous reports of this IL loaded with boron nanoparticles milled in [MAT][DCA] (**Table 1**).[34] After essentially the same ignition delay as the neat IL, the resulting ignition was more powerful with a higher flame (>10 cm) and a single combustion process (**Table 1**).

Taken together with our previous studies,[34] these results suggest that the surface functionalization of the boron nanoparticles is important in providing additional stability of the suspensions. The lower suspension stability of the H_2-milled vs. [MAT][DCA]-milled boron nanoparticles, must be balanced with the ease and lower cost of milling under H_2 vs. milling in ILs. The other conclusion is that the reactivity of the ILs with H_2-milled nanoparticles is not very different from ILs containing nanoparticles milled in the IL. It is not surprising that the ignition delays of these 0.3 wt% samples are not significantly different from those of the neat ILs, because the initial contact with the oxidizer is by the IL, rather than the suspended particles, and the boron presumably does not begin to oxidize until ignition of the IL exposes the particles. The fact that there are effects on flame height and duration suggest that the boron does enhance combustion, and this enhancement may involve both combustion of the boron, but also possible effects such as combustion catalysis on the particle surfaces and improvements in heating rates due to radiative heating of the particles (which appear black in higher concentration suspensions). To test the inherent combustibility of the boron particles, experiments at much higher particle loadings are needed.

Conclusion

Boron nanoparticles were prepared and loaded with hydrogen using ball milling, with the result that as much as 5 weight % (36 mole %) of hydrogen can be loaded into boron nanoparticles. Mass spectrometry and TGA experiments show that the incorporated hydrogen is stable up to ~100 °C. DFT calculations predict that hydrogen dissociatively adsorbs on the particle surfaces, mostly via terminal B−H bonds, and that interstitial binding is significantly higher in energy and therefore not likely to be important. FTIR experiments are consistent with this prediction, showing evidence only of terminal B−H covalent bonding, similar to that

observed in boranes. Mass spectroscopy and TGA-MS analyses show no evidence for formation of molecular boranes that are volatile in the temperature range probed.

Given that the boron-hydrogen binding appears to involve only B−H bonds to the surface, very high surface areas are required in order to account for the high hydrogen loadings observed. SEM and TEM suggest that the boron primary particles are small, with plate-like geometries that would, indeed, result in high surface areas. It appears that in H_2-milling the formation of a B−H layer on the boron surfaces acts to improve size reduction, by some combination of enhanced fracturing and reduced cold-welding probabilities.

Thermal desorption experiments showed that hydrogen desorbs mostly by recombination to produce H_2, with a smaller amount desorbing from oxidized samples as H_2O formed by recombination and desorption from hydrated oxides. Under inert atmosphere, most of the hydrogen desorbs from the boron below ~550 °C, although some hydrogen desorption is observed up to 900 °C. Together with the observation that H_2-milled boron also oxidizes more readily than boron without hydrogen loading, this result suggests that hydrogen-loaded boron might significantly improve ignition, and combustion, as well as providing a small increase in I_{sp}. Enhancements in flame height and duration suggest that the particles do burn during the hypergolic ignition of boron-IL suspensions.

Methods

Hydrogen loading and nanoparticle production. Boron powder feedstock (~95 %, 2 μm diameter) was purchased from C. R. Supply Co. (West Hills, CA) and used as received, although some experiments aimed at purifying the boron feedstock are discussed. Hydrogen loading was accomplished by milling boron powder in an H_2 atmosphere. In a typical milling procedure, 2 g of boron and 160 grams of 1/8 inch diameter tungsten carbide media were loaded

into a 500-mL tungsten carbide-lined milling jar. The jar lid was modified with two valved ports which allow the jar atmosphere to be pumped out, purged, filled, and sampled, without breaking the lid seal. After loading, the jar is sealed and then pumped out and purged with Ar three times, before finally pumping out the Ar and charging the jar with H_2 gas (99.95 % purity, Airgas USA, LLC, Denver, CO). For most experiments the absolute H_2 charge pressure was 60 psia (~4 atm). The reactants and the tungsten carbide media were milled using a PM 400 planetary ball mill (Retsch, Inc., Haan, Germany) for a total of 16 h at 300 RPM. The milling program consisted of 30-minute milling periods with 5 minute rest/cooling intervals, reversing the milling direction between each cycle. The pressure of H_2 inside the jar was monitored at intervals during the milling process by stopping the mill and connecting a gauge to one of the ports in the jar lid, pumping out the gauge, and then opening the valve to allow measurement of the internal pressure. For deuterium-loading experiments, the same set of procedures was employed with the use of D_2 gas instead of H_2. Control experiments were performed with H_2 as the jar atmosphere, but without boron added, and with boron but with argon as the milling atmosphere.

Unless noted, all manipulations of the boron, including loading and unloading the jar, and transfer of samples for various analyses, were performed in an N_2-filled glove box to minimize exposure to air. Gas sampling was also done inside the glovebox such that the jar atmosphere was never exposed to air.

Hydrogen content analysis. Hydrogen uptake was determined in two ways. The most straightforward was simply measuring the drop in H_2 pressure in the milling jar over the course of the milling run. This measurement allows the total hydrogen uptake to be calculated, but provides no insight into the form in which the hydrogen is bound, or whether the hydrogen remains bound when the H_2 overpressure is removed. Therefore, we also analyzed the hydrogen

loading of the resulting particles using a high-temperature-conversion elemental analyzer (TC/EA) coupled to a Thermo Finnigan Delta V Plus Isotope Ratio Mass Spectrometer (IRMS) (Thermo Fisher Scientific Inc., Waltham, MA) through an open split interface. For this analysis, a sample of the solid milling product was transferred to a sample vial, and from the vial a sample was dropped into a He carrier stream, which carried the sample through a 1400 °C glassy carbon pyrolytic reactor, desorbing any hydrogen as H_2. Gases are separated in a 1 meter long gas chromatography column (5A, 80 mL/min, 95 °C) before entering the IRMS for quantitation of the H_2. Ultrahigh purity H_2 was injected at appropriate times during analysis to ensure proper mass and sensitivity calibration. This instrument is not equipped for inert atmosphere sample transfer, therefore the sample was exposed to air briefly before analysis.

Electron Microscopy. Particle size and shape were analyzed using scanning electron microscopy (SEM-FEI Nova Nano 600, Hillsboro, OR). Samples for SEM were prepared by sonicating and dispersing the particles in ethanol to break up aggregates. Particles were then drop cast and dried on a transmission electron microscopy (TEM) grid, which was affixed to the SEM sample holder using carbon tape. These samples were exposed to air during transfer to the SEM. In addition, a scanning TEM was used to examine the particles. This analysis was done using a FEI Technai Osiris instrument (FEI Co., Hillsboro, OR) at 200 kV operation. Electron energy loss spectroscopy (EELS) was used to verify that the particles examined were boron.

Fourier Transform Infrared (FTIR) Analysis. A Nicolet iS5 FTIR spectrometer (Thermo Fisher Scientific, Waltham, MA) was used to collect infrared (IR) spectra using an attenuated total reflectance (ATR) set-up. Milled boron samples were directly pressed onto the instrument's diamond crystal. IR spectra were obtained with a resolution of 1 cm^{-1} in 15 independent scans, and then averaged.

Mass spectrometry analysis. After milling selected samples, headspace gas was analyzed using a quadrupole mass spectrometer system with base pressure below 10^{-8} mbar. The gas was sampled by connecting a sealed glass tube to the milling jar's valve port. To avoid N_2 introduction from the glove box atmosphere, the glass tube was first purged by pumping out and filling it with Ar repeatedly, before the headspace gas was collected. The glass tube was then valved off, and connected to the inlet system of the mass spectrometer. The dead volume between the valves on the sample tube and mass spectrometer inlet was evacuated, and then the valves were opened to allow headspace gas to enter the mass spectrometer ion source.

Mass spectra were also measured for gases evolved from samples of H_2- and D_2-loaded boron nanoparticles as they were heated. For these measurements, the jar was opened in the glove box, and a boron powder sample was collected and transferred into a glass sample tube equipped with a valve. The boron-filled tube was then connected to the mass spectrometer inlet manifold, and gases were continuously leaked into the instrument as the sample tube was slowly heated using a tube furnace, thereby obtaining mass spectra of gases evolving as the temperature was raised.

The detection sensitivity of mass spectrometers typically varies with mass, and for light gases like hydrogen, the effect can be substantial. To ensure that the compositions reported for the headspace and evolved gases are accurate, the sensitivity of the mass spectrometer used in these analyses was calibrated by measuring the intensities for H_2, D_2, and Ar, independently introduced into the mass spectrometer at constant pressure, as measured by an ionization gauge, and corrected for the gauge's detection sensitivity. The spectra presented below have been corrected for variation of sensitivity with mass.

Tandem thermogravimetric-mass spectrometry analysis (TGA-MS). Mass losses as a function of temperature were studied using a thermogravimetry instrument, also equipped with a mass spectrometer for analysis of the evolved gases. Samples were prepared and analyzed with a TA Model Q500 Thermogravimetric Analyzer operated inside a N_2-filled glovebox. Samples were heated from 25 °C to 900 °C at a constant temperature ramp rate of 10 °C/min under N_2 gas flow (90 mL/min). Mass analysis was done simultaneously with TGA by sampling the gas stream with a Pfeiffer ThermoStar GSD301T3 quadrupole mass spectrometer (Pfeiffer Vacuum, Nashua, NH) which allowed monitoring specific masses of interest as a function of sample temperature.

Oxidation of hydrogenated boron samples as a function of temperature was studied using a TA Model 2950 Thermogravimetric Analyzer (TA Instruments, New Castle, DE) operated outside the glovebox and flowing O_2 into the furnace and the sample balance. Because this TGA was located outside the glove box, the samples for oxidation analysis were, necessarily, exposed to air during transfer to the instrument. This instrument was not equipped with a mass spectrometer.

Theoretical Performance Calculation. One potential application is as a fuel additive in a bipropellant system propulsion system. The theoretical performance gain from hydrogen loading was estimated using the US Air Force specific impulse computational code.[30]

Density Functional Theory (DFT) calculations. The interactions between boron nanoparticles and hydrogen were computed using density functional theory (DFT) methods. A cluster of eighty boron atoms with both expose surface atoms and a bulk-like core[36,37] was used as a model for a boron nanoparticle. The M06 hybrid meta-generalized gradient approximation (GGA) exchange-correlation functional of Zhao and Truhlar[38] was used in conjunction with the

6-311++G(d,p) basis set[39,40] for boron and hydrogen, denoted as M06/6-311++G(d,p). All H_xB_{80} structures reported herein were fully optimized and verified as local minima or saddle points via diagonalization of the hessian matrix; i.e., the mass-weighted energy second derivatives with respect to nuclear displacements. A scale factor of 0.983[38] was used in computing infrared spectra and zero point vibrational energy corrections from the harmonic vibrational frequencies. All calculations were performed using the GAMESS[41,42] and NWChem[43] quantum chemistry programs.

Synthesis of Ionic Liquids. Two hypergolic ionic liquids (ILs, salts with melting points below 100 ^{o}C, which upon contact with white fuming nitric acid spontaneously ignite)[35] were synthesized in order to test the combustion properties of the hydrogenated boron nanoparticles. The IL precursors, 1-butyl-3-methyl-imidazolium chloride and 1-methyl-4-amino-1,2,4-triazolium iodide were synthesized through typical quaternization reactions between heterocycles (1-methyl-imidazole and 4-amino-1,2,4-triazole) and alkylating agents (1-chlorobutane and methyl iodide).[34] Halide precursors were dissolved in the minimum amount of methanol and silver dicyanamide was added and stirred for five days while covered with aluminum foil. The resulting silver halide salts were filtered and methanol was removed by reduced pressure to obtain 1-butyl-3-methyl-imidazolium dicyanamide ([BMIM][DCA]) and 1-methyl-4-amino-1,2,4-triazolium dicyanamide ([MAT][DCA]) as very slightly yellow liquids.[34,35] ILs were further dried at 70 ^{o}C for 7 days while under a mild vacuum (1 x 10^{-4} torr) until they contained less than 2000 ppm of water. 1-methyl-imidazole was purchased from Sigma-Aldrich (St. Louis, MO) and used as received. 4-amino-1,2,4-triazole, 1-chlorobutane, methyl iodide, silver nitrate, and sodium dicyanamide were purchased from Alfa Aesar (Ward Hill, MA) and used as received.

Stabilization of Hydrogenated Boron Nanoparticles in ILs. Small portions of hydrogenated and deuterated boron nanoparticles (0.6 − 0.9 mg) were placed in pre-weighed vials while under an Ar atmosphere. The corresponding amount of [BMIM][DCA] and [MAT][DCA] (1.999 – 2.991 g) was added to the vials in a Vacuum Atmospheres Company (Hawthorne, CA) Omni-Lab glovebox to obtain 0.3 wt% suspensions under an inert Ar atmosphere. Mixtures were then sealed, brought out of the glovebox, and vortex mixed and stirred as initial attempt to disperse the particles. Unfortunately, successful dispersion was not achieved through this process. A more powerful ultrasonication process using a Branson 5510 bath sonicator was used to achieve complete dispersion. The vials were sonicated for four consecutive 99-minute cycles until no particles were visible along the edges of the vials as described in an identical suspension procedure from a previous work.[34] In each case, the suspensions produced a cloudy yellow color. Aggregated samples could be resuspended by repeating the original sonication procedure.

Hypergolic Ignition Tests. In order to determine the combustion and ignition properties of the hydrogenated boron nanoparticles, neat samples of hypergolic ILs were compared to samples of hypergolic ILs containing 0.3% wt of hydrogenated boron nanoparticles. Aliquots (10 μL) of neat ILs or ILs loaded with boron nanoparticles were added via Hamiltonian syringe to a flat bottom vial containing 500 μL of 99% white fuming nitric acid, which followed our previously reported procedures.[34] The reaction was monitored for ignition delay (defined as the time from when the drop of IL hits the surface of the oxidizer until the resulting ignition), flame height, and ignition dynamics utilizing a Redlake (Tallahassee, FL) MotionPro Y4 high speed camera at 1000 frames/s. Each test was repeated a total of three times to determine repeatability.

Acknowledgements

The authors acknowledge support from the Air Force Office of Scientific Research under AFOSR MURI Grant FA9550-08-1-0400 and BRI Grant FA9550-12-1-0481, and from the University of Utah Research Foundation (grant 51003387). This work made use of University of Utah shared facilities of the Micron Microscopy Suite sponsored by the College of Engineering, Health Sciences Center, Office of the Vice President for Research, and the Utah Science Technology and Research (USTAR) initiative of the State of Utah. The AFRL group would like to acknowledge the Department of Defense High Performance Computing Modernization Program at the Air Force Research Laboratory, Engineering Research and Development Center, and Navy DoD Supercomputing Resource Centers for the computer time granted for the theoretical work. The University of Alabama group would like to thank the Air Force Office of Scientific Research (AFOSR Grant # FA9550-10-1-0521) and PDM thanks the United States Department of Defense (DoD) through the National Defense, Science & Engineering Graduate Fellowship (NDSEG) Program.

Conflict of Interest Disclosure

The authors declare no competing financial interest.

Supporting Information

Additional data. This material is available free of charge via the Internet at http://pubs.acs.org.

References

1. Cox, J. D.; Wagman, D. D.; Medvedev, V. A.; Hemisphere Publishing Corp: 1984.

2. Plantier, K. B.; Pantoya, M. L.; Gash, A. E. Combustion Wave Speeds of Nanocomposite Al/Fe_2o_3: The Effects of Fe_2o_3 Particle Synthesis Technique *Combust. Flame* **2005**, *140*, 299-309.

3. Armstrong, R. W.; Baschung, B.; Booth, D. W.; Samirant, M. Enhanced Propellant Combustion with Nanoparticles. *Nano Lett* **2003**, *3*, 253-255.

4. Wang, L. L.; Munir, Z. A.; Maximov, Y. M. Review Thermite Reactions: Their Utililzation in the Synthesis and Processing of Materials. *J. Mat. Sci.* **1993**, *28*, 3693-3708.

5. Van Devener, B.; Perez, J. P. L.; Anderson, S. L. Air-Stable, Unoxidized, Hydrocarbon-Dispersible Boron Nanoparticles. *J. Mat. Res.* **2009**, *24*, 3462-3464.

6. Van Devener, B.; Perez, J. P. L.; Jankovich, J.; Anderson, S. L. Oxide-Free, Catalyst-Coated, Fuel-Soluble, Air-Stable Boron Nanopowder as Combined Combustion Catalyst and High Energy Density Fuel. *Energy Fuels* **2009**, *23*, 6111-6120.

7. Perez, J. P. L.; McMahon, B. W.; Schneider, S.; Boatz, J. A.; Hawkins, T. W.; McCrary, P. D.; Beasley, P. A.; Kelley, S. P.; Rogers, R. D.; Anderson, S. L. Exploring the Structure of Nitrogen-Rich Ionic Liquids and Their Binding to the Surface of Oxide-Free Boron Nanoparticles. *J. Phys. Chem. C* **2013**, *117*, 5693-5707.

8. Perez, J. P. L.; McMahon, B. W.; Anderson, S. L. Functionalization and Passivation of Boron Nanoparticles with a Hypergolic Ionic Liquid. *J. Propul. Power* **2013**, *29*, 489-495.

9. Dequasie, A. T. *The Green Flame: Surviving Government Secrecy*; American Chemical Society: Washington, DC, 1991.

10. Eberle, U.; Felderhoff, M.; Schueth, F. *Angew. Chem. Int. Ed.* **2009**, *48*, 6608-6630.

11. Khalil, A. E. E.; Gupta, A. K. Hydrogen Addition Effects on High Intensity Distributed Combustion. *Appl. Energ.* **2013**, *104*, 71-78.

12. Weng, Q.; Wang, X.; Zhi, C.; Bando, Y.; Golberg, D. Boron Nitride Porous Microbelts for Hydrogen Storage. *ACS Nano* **2013**, *7*, 1558-1565.

13. Wang, P.; Orimo, S.; Tanabe, K.; Fujii, H. Hydrogen in Mechanically Milled Amorphous Boron. *J. Alloys Compd.* **2003**, *350*, 218-221.

14. Tilton, J. A.; Smith, W. M.; Hockerberger, W. G. Production of High Cetane Number Diesel Fuels by Hydrogenation. *Ind. Eng. Chem. Res.* **1948**, *40*, 1269-1273.

15. Ji, C.; Wang, S.; Zhang, B. Performance of a Hybrid Hydrogen–Gasoline Engine under Various Operating Conditions. *Appl. Energ.* **2012**, *97*, 584-589.

16. Clayton, R. M. Hydrogen Enrichment for Low-Emission Jet Combustion. *Adv. Chem. Ser.* **1978**, *166*, 267-286.

17. Ghenai, C.; Zbeeb, K.; Janajreh, I. Combustion of Alternative Fuels in Vortex Trapped Combustor. *Energy Convers. Manage.* **2013**, *65*, 819-828.

18. Ma, F.; Wang, Y.; Liu, H.; Li, Y.; Wang, J.; Zhao, S. Experimental Study on Thermal Efficiency and Emission Characteristics of a Lean Burn Hydrogen Enriched Natural Gas Engine. *Int. J. Hydrogen Energy* **2007**, *32*, 5067-5075.

19. Guo, H.; Hosseini, V.; Neill, W. S.; Chippior, W. L.; Dumitrescu, C. E. An Experimental Study on the Effect of Hydrogen Enrichment on Diesel Fueled Hcci Combustion. *Int. J. Hydrogen Energy* **2011**, *36*, 13820-13830.

20. *Department of Energy Hydrogen and Fuel Cells Program Plan*, U.S. Department of Energy, 2011.

21. Huang, Z.; Calka, A.; Liu, H. Dsc Study of the Effect of Milling Conditions on the Hydrogen Storage Properties of Boron. *J. Mat. Sci.* **2007**, *42*, 3985-3989.

22. Kobayashi, M.; Higashi, I.; Takami, M. Fundamental Structure of Amorphous Boron. *J. Solid State Chem.* **1997**, *133*, 211-214.

23. Moulder, J. F.; Stickle, W. F.; Sobol, P. E.; Bomben, K. D.; J. Chastain & R. C. King, J., eds. *Handbook of X-Ray Photoelectron Spectroscopy*; Physical Electronics: Eden Prarie, MN, 1995.

24. Peak, D.; Luther, G. W. I.; Sparks, D. L. Atr-Ftir Spectroscopic Studies of Boric Acid Adsorption on Hydrous Ferric Oxide. *Geochim. Cosmochim. Acta* **2003**, *67*, 2551-2560.

25. Linstrom, P. J.; Mallard, W. G.; National Institute of Standards and Technology: Gaithersburg MD, 20899, 2011.

26. Yaws, C. L. *Handbook of Vapor Pressure*; Gulf Publishing Co.: Houston, TX, 1995; Vol. 4.

27. Balcı, S.; Sezgi, N. A.; Eren, E. Boron Oxide Production Kinetics Using Boric Acid as Raw Material. *Ind. Eng. Chem. Res.* **2012**, *51*, 11091-11096.

28. Roth, W.; Bauer, W. H. The Explosive Oxidation of Diborane. *J. Phys. Chem.* **1956**, *60*, 639-641.

29. Ludlum, K. H.; Wiberley, S. E.; Bauer, W. H. The Oxidation of Tetraborane, Rensselaer Polytechnic Institute, 1961.

30. Beckman; Acree; U.S. Air Force Research Laboratory: Edwards AFB, CA, 1990.

31. Sutton, G. P. *Rocket Propulsion Elements*; 6th ed.; Wiley: New York, 1992.

32. Johnson, W. H.; Kilday, M. V.; Prosen, E. J. Heat of Formation of Decaborane. *J. Res. Natl. Bur. Stand., Sec. A* **1960**, *64A*, 521-525.

33. Edwards, T. Liquid Fuels and Propellants for Aerospace Propulsion: 1903-2003. *J. Propul. Power* **2003**, *19*, 1089-1107.

34. McCrary, P. D.; Beasley, P. A.; Cojocaru, O. A.; Schneider, S.; Hawkins, T. W.; Perez, J. P. L.; McMahon, B. W.; Pfiel, M.; Boatz, J. A.; Anderson, S. L.; Son, S. F.; Rogers, R. D. *Chem. Comm.* **2012**, *48*, 4311-4313.

35. Schneider, S.; Hawkins, T.; Rosander, M.; Vaghjiani, G.; Chambreau, S.; Drake, G. *Energy Fuels* **2008**, *22*, 2871-2872.

36. Zhao, J.; Wang, L.; Li, F.; Chen, Z. B80 and Other Medium-Sized Boron Clusters: Core−Shell Structures, Not Hollow Cages. *J. Phys. Chem. A* **2010**, *114*, 9969-9972.

37. Li, F.; Jin, P.; Jiang, D.; Wang, L.; Zhang, S. B.; Zhao, J.; Chen, Z. B80 and B101–103 Clusters: Remarkable Stability of the Core-Shell Structures Established by Validated Density Functionals. *J.Chem. Phys.* **2012**, *136*, 074302-074311.

38. Zhao, Y.; Truhlar, D. G. The M06 Suite of Density Functionals for Main Group Thermochemistry, Thermochemical Kinetics, Noncovalent Interactions, Excited States, and Transition Elements: Two New Functionals and Systematic Testing of Four M06-Class Functionals and 12 Other Functionals. *Theor. Chem. Acc.* **2008**, *120*, 215-241.

39. Krishnan, R.; Binkley, J. S.; Seeger, R.; Pople, J. A. Self-Consistent Molecular Orbital Methods. Xx. A Basis Set for Correlated Wave Functions. *J.Chem. Phys.* **1980**, *72*, 650-654.

40. Clark, T.; Chandrasekhar, J.; Spitznagel, G. W.; Schleyer, P. v. R. Efficient Diffuse Function-Augmented Basis Sets for Anion Calculations. Iii. The 3-21+G Basis Set for First-Row Elements, Li–F. *J. Comput. Chem.* **1983**, *4*, 294-301.

41. Schmidt, M. W.; Baldridge, K. K.; Boatz, J. A.; Elbert, S. T.; Gordon, M. S.; Jensen, J. H.; Koseki, S.; Matsunaga, N.; Nguyen, K. A.; Su, S.; Windus, T. L.; Dupuis, M.; Montgomery, J.

A. General Atomic and Molecular Electronic Structure System. *J. Comput. Chem.* **1993**, *14*, 1347-1363.

42. Gordon, M. S.; Schmidt, M. W. *Theory and Applications of Computational Chemistry: The First Forty Years*; Elsevier: Amsterdam, 2005.

43. Valiev, M.; Bylaska, E. J.; Govind, N.; Kowalski, K.; Straatsma, T. P.; van Dam, H. J. J.; Wang, D.; Nieplocha, J.; Apra, E.; Windus, T. L.; de Jong, W. A. Nwchem: A Comprehensive and Scalable Open-Source Solution for Large Scale Molecular Simulations. *Comput. Phys. Commun.* **2010**, *181*, 1477-1489.

Tables and Figures

Table Title

Table 1: Summary of ignition and combustion properties of neat [BMIM][DCA] and [MAT][DCA] ILs, and the same ILs with several types of boron nanoparticles added at 0.3 % loading. The numbers in parentheses following the ignition delay and duration values are the standard deviations of multiple runs. The results for H_2-loaded boron particles are compared to previous work for the same ILs loaded with non-hydrogenated boron nanoparticles, with and without capping by either a hydrocarbon ligand or by [MAT][DCA].[32]

Figure Captions

Figure 1: **(a.)** Pressure drop of H_2 inside the jar measured at different intervals during the milling. **(b.)** H_2 consumed during the milling as weight percent of boron loading.

Figure 2: Reaction pathway and energy diagram for the interaction of an H_2 molecule with a B80 cluster.

Figure 3: FTIR spectrum of hydrogenated boron nanoparticles produced after milling.

Figure 4: B 1s Region XPS of H_2-milled **(top)** and Ar-milled **(bottom)** boron nanoparticles exposed to air prior to analysis.

Figure 5: SEM images of boron nanoparticles produced from dry milling in **(a.)** H_2 atmosphere, and **(b.)** Ar atmosphere. **(c.)** TEM image of boron nanoparticle milled in H_2.

Figure 6: Mass spectrum of headspace gas collected from the jar after milling for 16 h.

Figure 7: Mass spectra of gases evolved from deuterated boron nanoparticles heated to 350 °C.

Figure 8: TGA profile of deuterated boron nanoparticles with corresponding desorption signal of H_2O, D_2O, and D_2 monitored through the run. TGA analysis was done inside a glovebox under inert atmosphere.

Figure 9: TGA analysis of boron milled in H_2 and Ar run under O_2 atmosphere.

Table 1: Summary of ignition and combustion properties of neat [BMIM][DCA] and [MAT][DCA] ILs, and the same ILs with several types of boron nanoparticles added at 0.3 % loading. The numbers in parentheses following the ignition delay and duration values are the standard deviations of multiple runs. The results for H_2-loaded boron particles are compared to previous work for the same ILs loaded with non-hydrogenated boron nanoparticles, with and without capping by either a hydrocarbon ligand or by [MAT][DCA].[32]

Compound	Colloidal Stability (h)	Ignition Delay[a] (ms)	Ignition Duration (ms)	Notes
[BMIM][DCA] 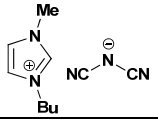	N/A	41(1)[b]	110(40)	One Flame – Medium
0.3% B-H_2	24	42(2)	159(56)	Two Flames – Medium and Medium
Neat [BMIM][DCA][a]	N/A	44(2)	106(6)	One Flame – Medium
0.33% B no ligand[a]	<24	44(3)	108(41)	One Flame – Very weak
0.33% B surfactant[a]	24	43(3)	110(50)	Two Flames – Medium
0.33% B [MAT][DCA][a]	48	44(3)	130(31)	Three Flames – Medium and High
[MAT][DCA] 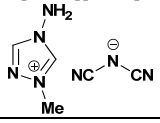	N/A	34(10)	59(10)	One Flame – Medium
0.3% B-H_2	36	34(2)	87(10)	One Flame – Very Strong
Neat [MAT][DCA][a]	N/A	37(6)	77(18)	One Flame – Medium
0.33% B no ligand[a]	<24	43(9)	52(12)	One/Two Flames – Very weak
0.33% B surfactant[a]	24	45(11)	56(7)	One Flame - Medium
0.33% B [MAT][DCA][a]	48	45(14)	43(4)	One Flame – Very Strong

[a]Data from table taken from Ref 32

Figure 1: (a.) Pressure drop of H_2 inside the jar measured at different intervals during the milling. **(b.)** H_2 consumed during the milling as weight percent of boron loading.

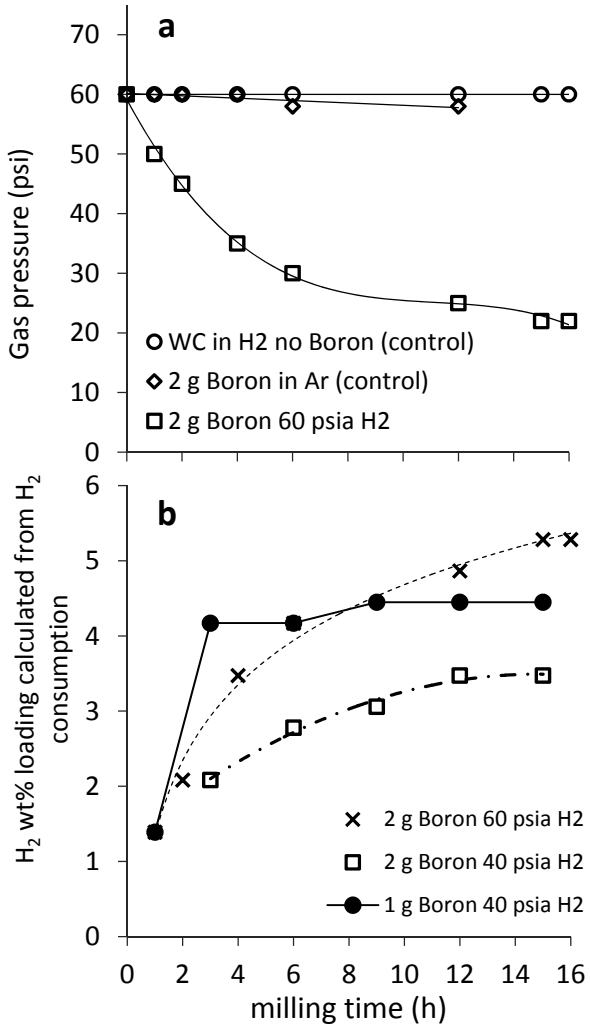

Figure 2: Reaction pathway and energy diagram for the interaction of an H_2 molecule with a B_{80} cluster.

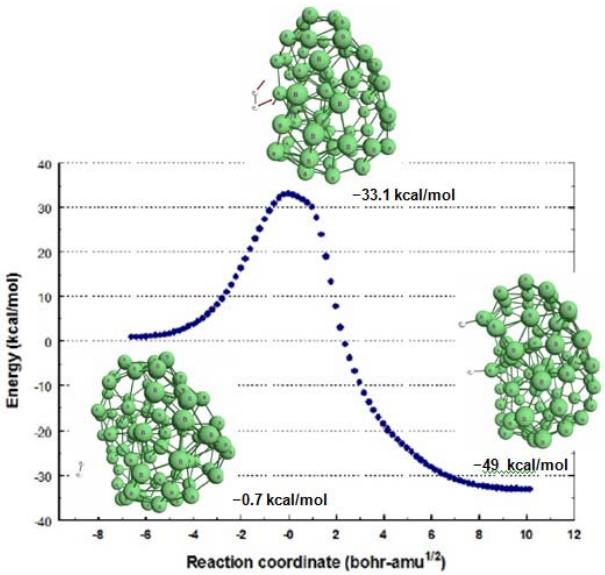

Figure 3: FTIR spectrum of hydrogenated boron nanoparticles produced after milling.

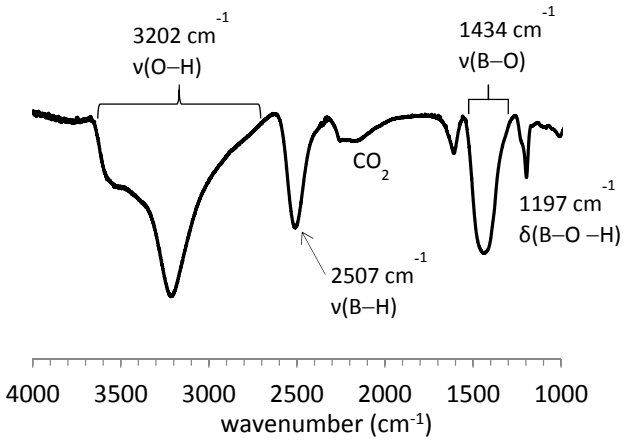

Figure 4: B 1s Region XPS of H_2-milled (**top**) and Ar-milled (**bottom**) boron nanoparticles exposed to air prior to analysis.

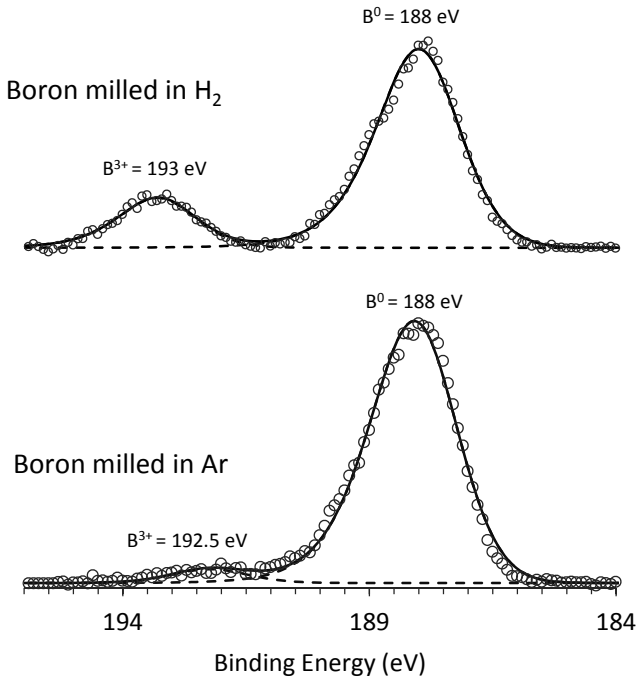

Figure 5: SEM images of boron nanoparticles produced from dry milling in **(a.)** H_2 atmosphere, and **(b.)** Ar atmosphere. **(c.)** TEM image of boron nanoparticle milled in H_2.

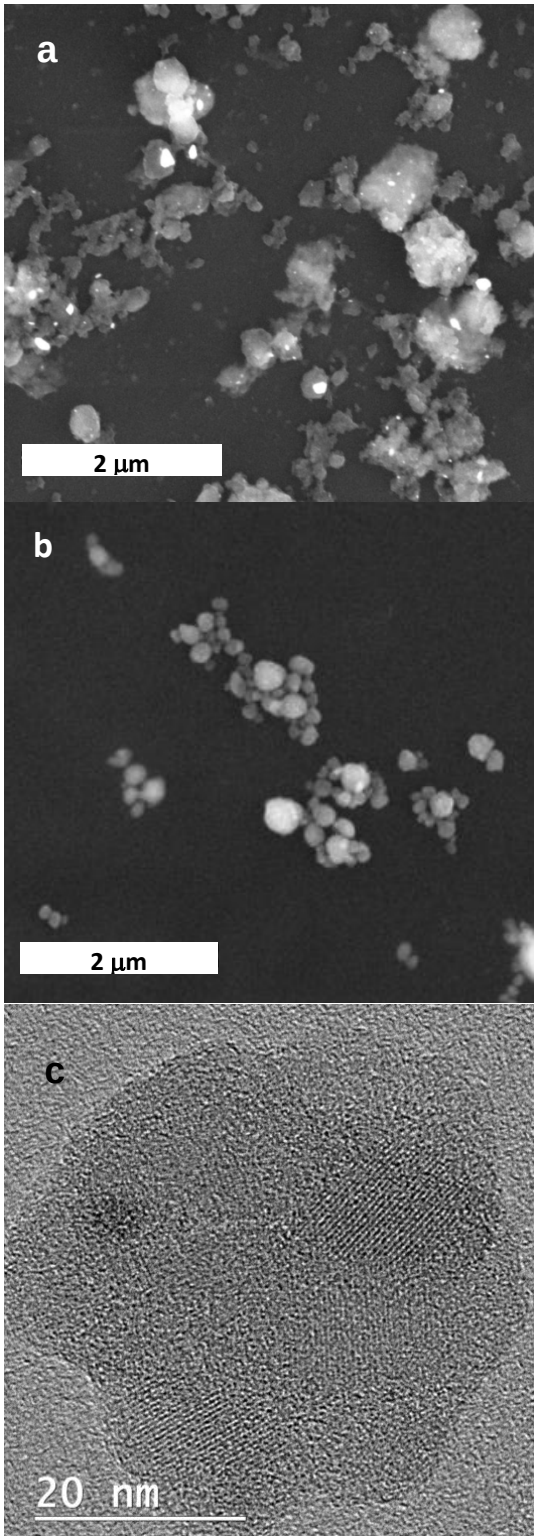

Figure 6: Mass spectrum of headspace gas collected from the jar after milling for 16 h.

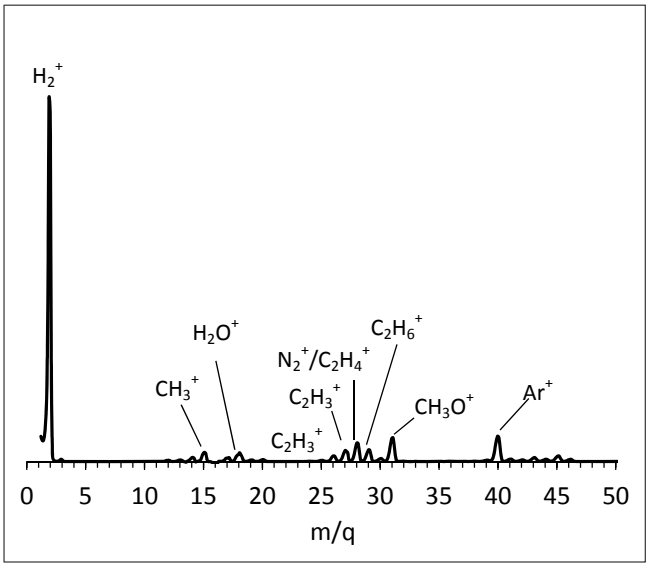

Figure 7: Mass spectra of gases evolved from deuterated boron nanoparticles heated to 350 °C.

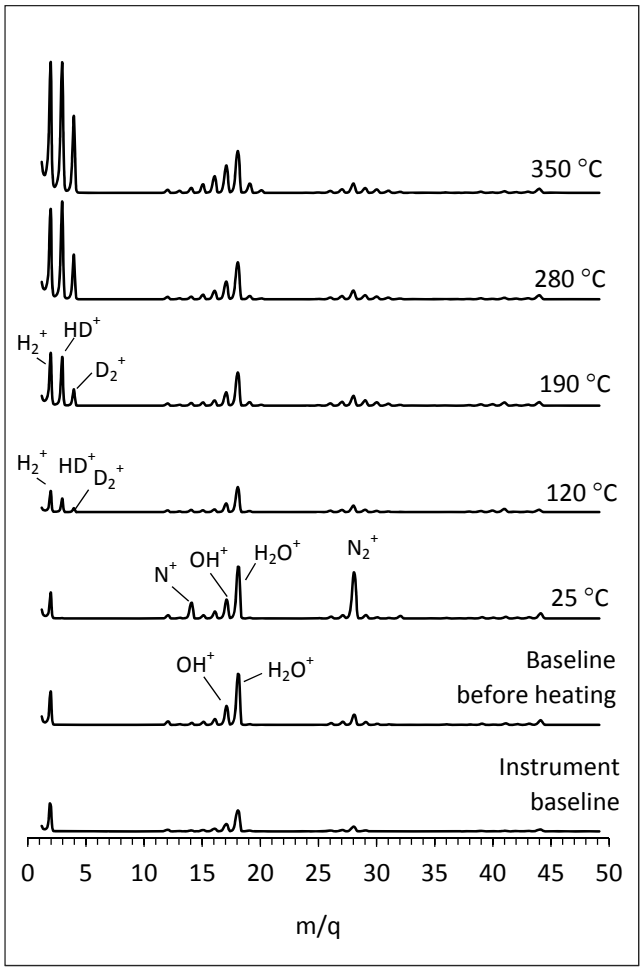

Figure 8: TGA profile of deuterated boron nanoparticles with corresponding desorption signal of H_2O, D_2O, and D_2 monitored through the run. TGA analysis was done inside a glovebox under inert atmosphere.

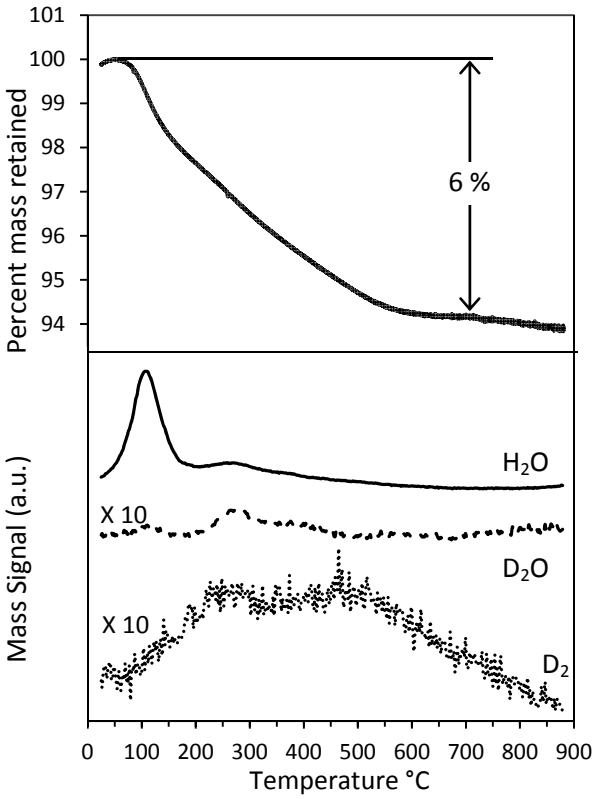

Figure 9: TGA analysis of boron milled in H_2 and Ar run under O_2 atmosphere.

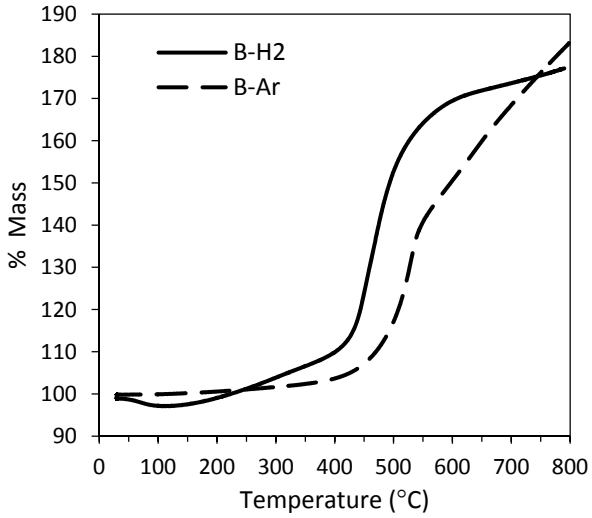

TOC only

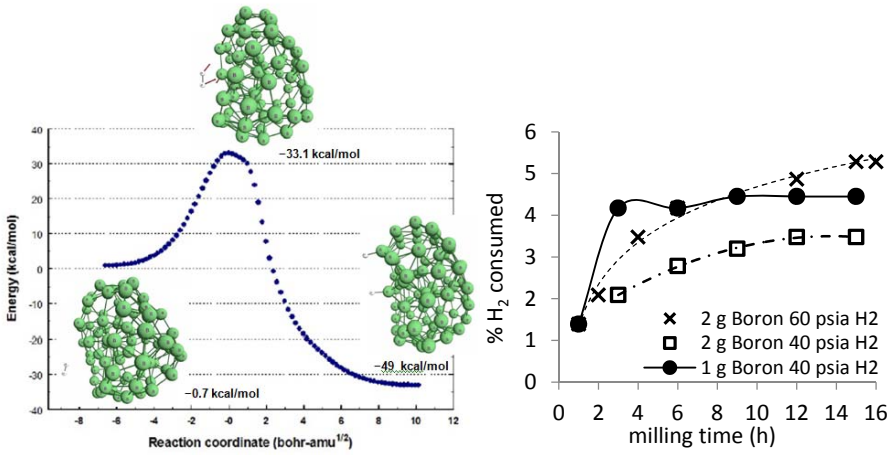

Electronic Supporting Information

Boron Nanoparticles with High Hydrogen Loading: Mechanism for B−H Binding, Size Reduction, and Potential for Improved Combustibility and Specific Impulse

Jesus Paulo L. Perez[†], Brandon W. McMahon[†], Jiang Yu[†], Stefan Schneider[‡], Jerry A. Boatz[‡], Tom W. Hawkins[‡], Parker D. McCrary[§], Luis A. Flores[§], Robin D. Rogers[§] and Scott L. Anderson[†*]

[†] *Department of Chemistry, University of Utah, 315 S 1400 E, Salt Lake City, UT 84112, USA;*

[‡] *Propellants Branch, Rocket Propulsion Division, Aerospace Systems Directorate, Air Force Research Laboratory, AFMC AFRL/RQRP, 10 E Saturn Blvd, Edwards AFB, CA 93524, USA*

[§] *Center for Green Manufacturing and Department of Chemistry, The University of Alabama, Tuscaloosa, AL 35487, USA*

* Corresponding author. E-mail: anderson@chem.utah.edu

Concentration of Boron Surface Sites as a Function of Particle Size.

The ~5 wt% hydrogen loading observed for H_2-milled boron nanoparticles corresponds to a B:H atom ratio of ~1.8:1, i.e., more than one H atom for every two boron atoms in the sample. In boranes, stoichiometries vary from 1:3 for diborane, to 1:1.4 for decaborane.[1] The larger boranes tend to be cage-like, with a single H atom per B atom, except at edges, where there can be two H/B. Therefore, one reasonable hypothesis about the hydrogen binding is to assume that boron atoms on the surface of boron nanoparticles might accommodate one H atom. In that case, 1.8:1 B:H ratio implies that ~56 % of the boron atoms must be in the surface layer.

Here we estimate the size that would be required to give 56 % surface atoms if the particles were uniform spheres, with density equal to the density of bulk amorphous boron (2.37 g/cm^3),[2] equivalent to 132 B atoms/nm^3. **Figure S1** shows the percent of the boron atoms in the surface layer, as a function of the particle diameter. It can be seen that for spherical particles, the diameter would need to be ~2 nm to have 56% of the atoms in the surface layer. In reality, the particles are larger, but also quite rough, with plate-like structure, as shown in **Figure 4** of the main manuscript.

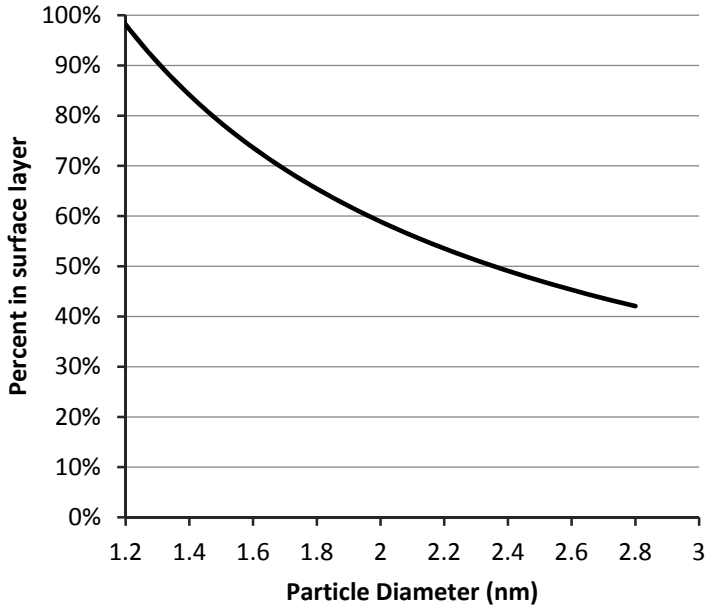

Figure S1. Plot of the percentage of boron atoms present on the surface as the particle size decreases.

Sampling depth of XPS

The extent of boron oxidation when samples were exposed to air was tested by X-ray photoelectron spectroscopy (XPS). **Figure 4** of the main manuscript shows the B 1s region scan of boron nanoparticle samples produced from dry milling in either H_2 or Ar atmospheres. The peak at 188 eV is due to elemental boron in the core of the particles, and the higher binding energy peak in each spectrum is due to oxidized boron on the surface of the samples. The B^{3+}/B^0 ratio is ~4 % for the Ar-milled sample, and is ~20 % in the H_2-milled sample. The effective attenuation length (EAL) for ~190 eV photoelectrons in solid boron is ~3 nm, and the EAL in boron oxide is similar.[3] The probability (P_{detect}) of detecting a photoelectron emitted at depth = z, is given by $P_{detect} = \exp(-z/EAL)$, thus most of the XPS signal comes from the top ~6 nm of the sample.

Density Functional Theory Calculations of the Interaction of Hydrogen with Boron, as Modeled by a B_{80} cluster

Results of DFT calculations at the M06/6-311++G(d,p) level, using a Lebedev integration grid of 99 radial and 590 angular points, are displayed in **Figures S2-S18**. **Figures S3-S9** and **S11** illustrate relative electronic energies (blue circles) along portions of the intrinsic reaction coordinate for the indicated reaction. The relative enthalpies of the fully optimized stationary points in **Figures S3-S12** and **S14** include scaled harmonic zero point vibrational energy corrections. The zero of energy is H_2 plus B_{80} at infinite separation, unless otherwise indicated.

The M06/6-311++G(d,p) optimized structure of B_{80} is shown in **Figure S2** and is similar to core-shell structures of B_{80} previously reported.[5-6] The addition and dissociation of a single H_2 molecule, and subsequent migration of H atoms on the surface of B_{80} follows different pathways as shown in **Figure S3 – S9**. In a typical reaction such as in **Figure S3a**, the structure of the reactants shows that H_2 is bound to the boron cluster by less than 1 kcal/mol and the closest H−B distance is greater than 2.9 angstroms. The transition state structure and displacement vector corresponding to the single imaginary vibrational frequency of 704i cm^{-1} for the dissociation of H_2 and subsequent formation of two B−H bonds on the surface of the B_{80} cluster is shown in the figure as well. The structure shown for the product represents the optimized geometry of H_2B_{80}. A portion of the intrinsic reaction coordinate (IRC)[7-12] showing the energy profile of the reactant, the transition state, and the product is also included in the figure. These reaction pathways display the different energy profiles observed for the formation of terminal B−H bonds (**Figure S3**), bridging B −H−B bond (**Figure S4**), and the migration of H atoms on the surface (**Figure S5 – S9**) to form stable products. Different isomers of the H_2B_{80} product are shown in **Figure S10** together with their corresponding energies. In general, the addition of molecular H_2 to the B_{80} cluster to form the dihydride H_2B_{80} product is exothermic by as much as 60 kcal/mol, but encounters a barrier as high as 33 kcal/mol.

In order to examine the possibility of molecular hydrogen being trapped within the interior of the B_{80} cluster, the geometry of $H_2@B_{80}$, was optimized and confirmed as a local minimum, with the final structure shown in **Figure S11**. As seen in this figure, the hydrogen molecule is coordinated to a single boron atom. The H−H bond is stretched to 0.88 angstroms and each B−H distance is approximately 1.30 angstroms. $H_2@B_{80}$ is less stable than separated H_2 plus B_{80} by 62.7 kcal/mol, indicating that formation of this species is energetically unfavorable and therefore unlikely to occur.

Next, the effects of saturating the surface of the B_{80} cluster with atomic hydrogen were examined by calculating the geometry of H_xB_{80} (x = 58, 60). The optimized geometry of these species is illustrated in **Figure S12** and **S14**. An interesting observation for these structures is the increased formation of B−H−B bridge bonding, although terminal bonds still predominate.

Insertion of a molecule of hydrogen into an interior site of $H_{58}B_{80}$ leads to a structure ($H_2@H_{58}B_{80}$) that is 74 kcal/mol less stable than the separated H_2 and $H_{58}B_{80}$ (**Figure S13**). For $H_2@H_{60}B_{80}$ (**Figure S15**), the local geometry of the interior hydrogen molecule is qualitatively similar to that in $H_2@B_{80}$ (**Figure S11**). Specifically, the hydrogen molecule in $H_2@H_{60}B_{80}$ is coordinated to a single boron atom, with each B−H distance approximately 1.3 angstroms. However, the molecular H−H bond in $H_2@H_{60}B_{80}$ is stretched to 0.82 angstroms, which is 0.06 angstroms less than in the case of $H_2@B_{80}$. $H_2@H_{60}B_{80}$ is ~28 kcal/mol less stable than separated H_2 plus $H_{60}B_{80}$.

Comparison of the results for $H_2@B_{80}$ and $H_2@H_{60}B_{80}$ indicates that H_xB_{80} is better able to accommodate an interstitial H_2 molecule than B_{80}. That is, the smaller distortion of the H−H bond in $H_2@H_{60}B_{80}$ relative to $H_2@B_{80}$, plus the reduced energy penalty for addition of H_2 to an interior site (28 and 63 kcal/mol in $H_2@H_{60}B_{80}$ and $H_2@B_{80}$, respectively) reveal that saturation of the surface of the B_{80} cluster with atomic hydrogen increases the likelihood of interstitial trapping of H_2. However, upon further analysis, it was found out that the reverse migration of an interstitial H to the surface has a much lower energy barrier (~8 kcal/mol) which suggests that the existence of interstitial H is unstable and the formation of B−H bonds highly unlikely.

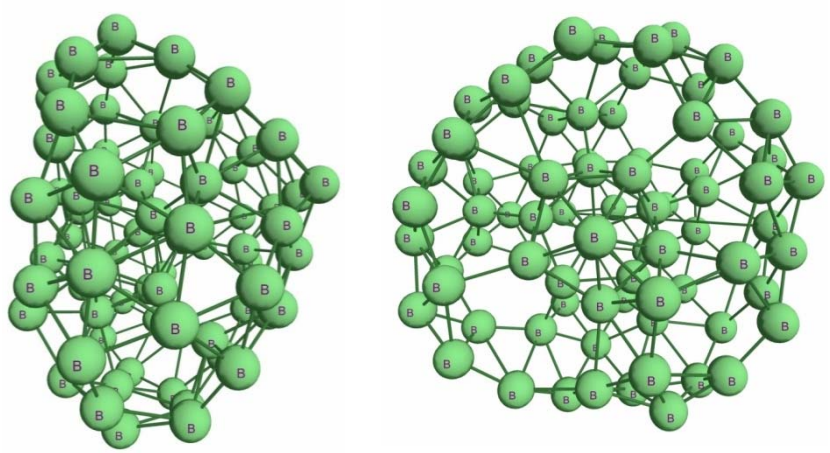

Figure S2. Two views of the M06/6-311+G(d,p) optimized geometry of the B_{80} core-shell nanocluster.

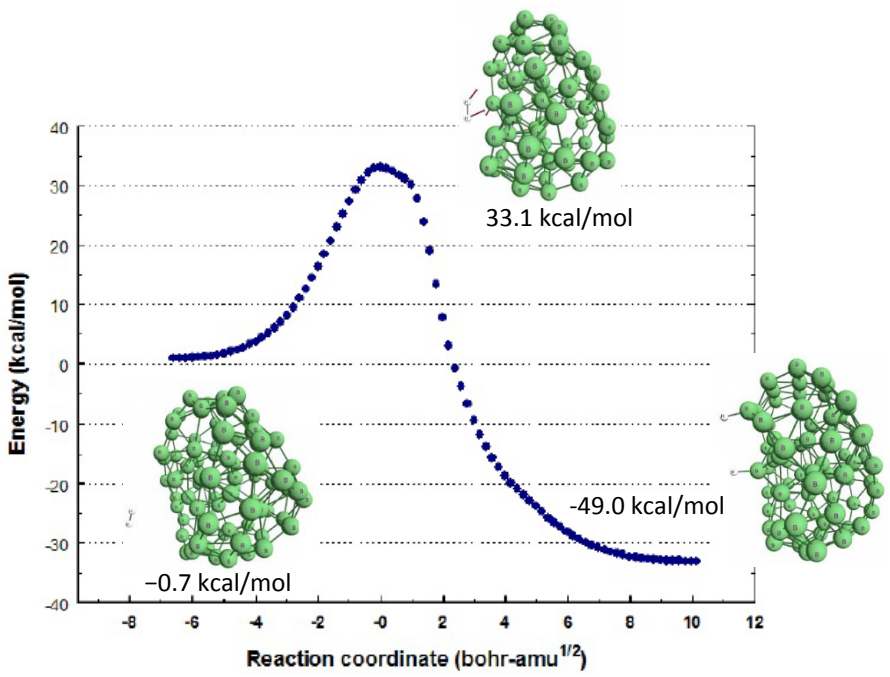

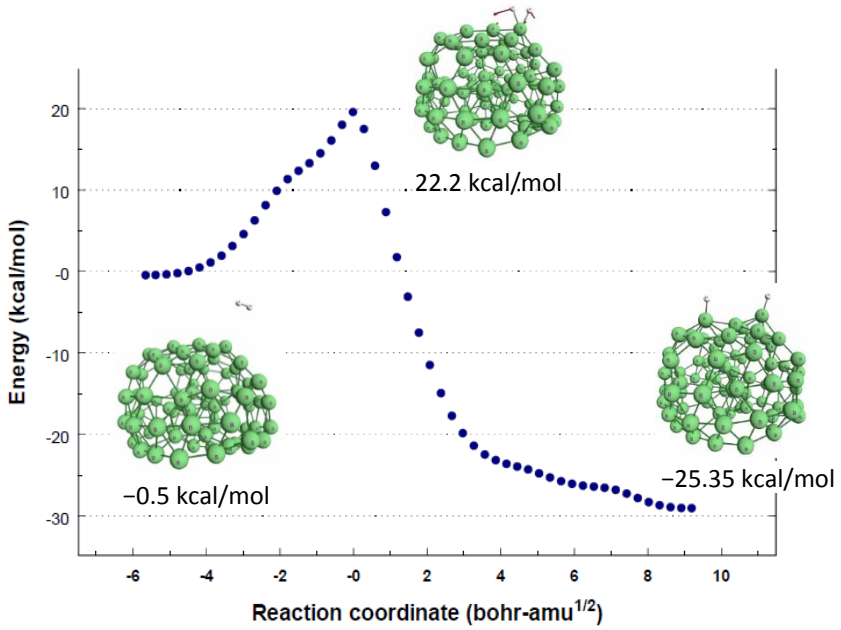

Figure S3. Two different reaction pathways for single-step 1,2 addition of H_2 to B_{80} forming H_2B_{80}. In **(a)** the two hydrogen atoms approch two different boron atoms on the surface to form a weakly bound H_2-B_{80} complex, which then dissociately chemisorbs on the surface, with the two H atoms on adjacent B atoms. The final product is more stable than the reactant by 48 kcal/mol and the reaction has a forward barrier of 34 kcal/mol. **(b)** H_2 approaches a single boron atom at the saddle point, then discociates to bind on adjacent B atoms. The product is more stable than the reactant by 25 kcal/mol but this reaction has a smaller forward barrier than **(a)**.

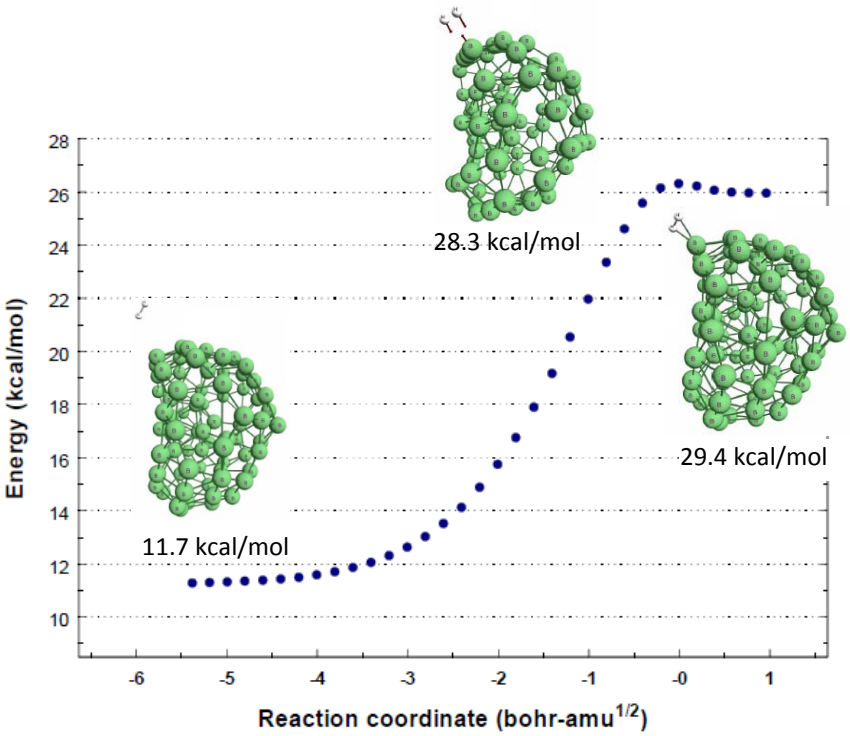

Figure S4. Reaction pathway for a single-step 1,1 addition of H_2 to B_{80} forming H_2 bound to a single B atom on the surface. The final product is less stable than the reactants and is only 1 kcal/mol more stable than the transition state.

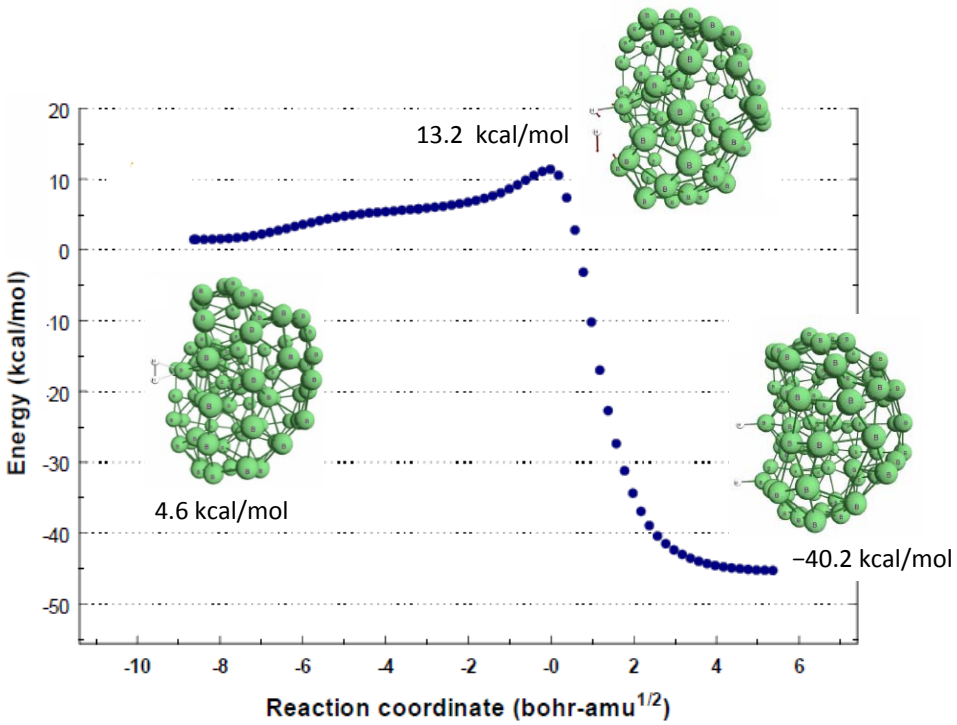

Figure S5. Reaction pathway for the migration of H atom on the B_{80} surface. Formation of a 1,2 B−H complex from a metastable 1,1 complex is 35 kcal/mol more stable with ~10 kcal/mol barrier.

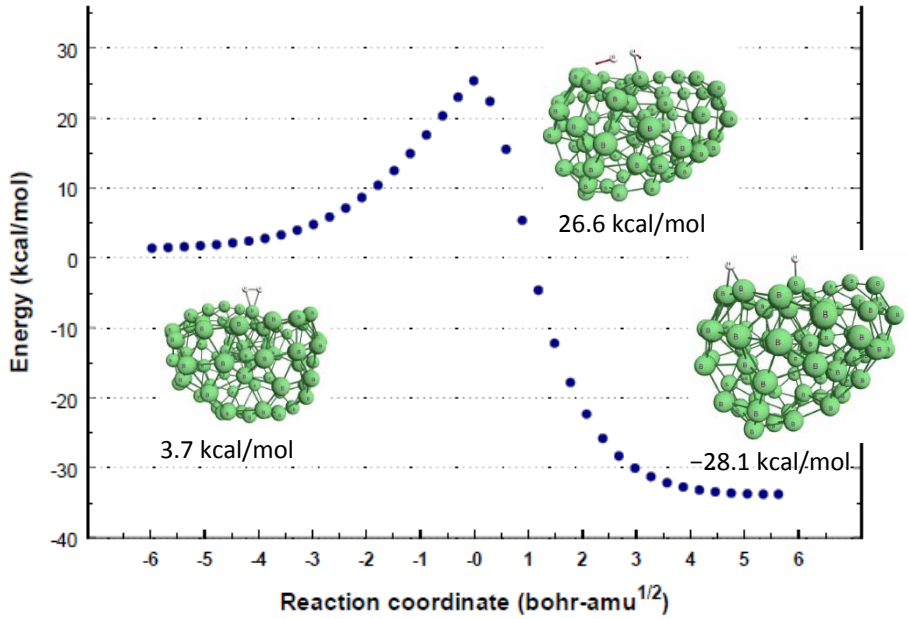

Figure S6. Reaction pathway for the migration of H atom on the B_{80} surface. The reaction forms a 1,2 product where one of the H atoms forms a terminal B−H bond and a bridging bond (B−H−B).

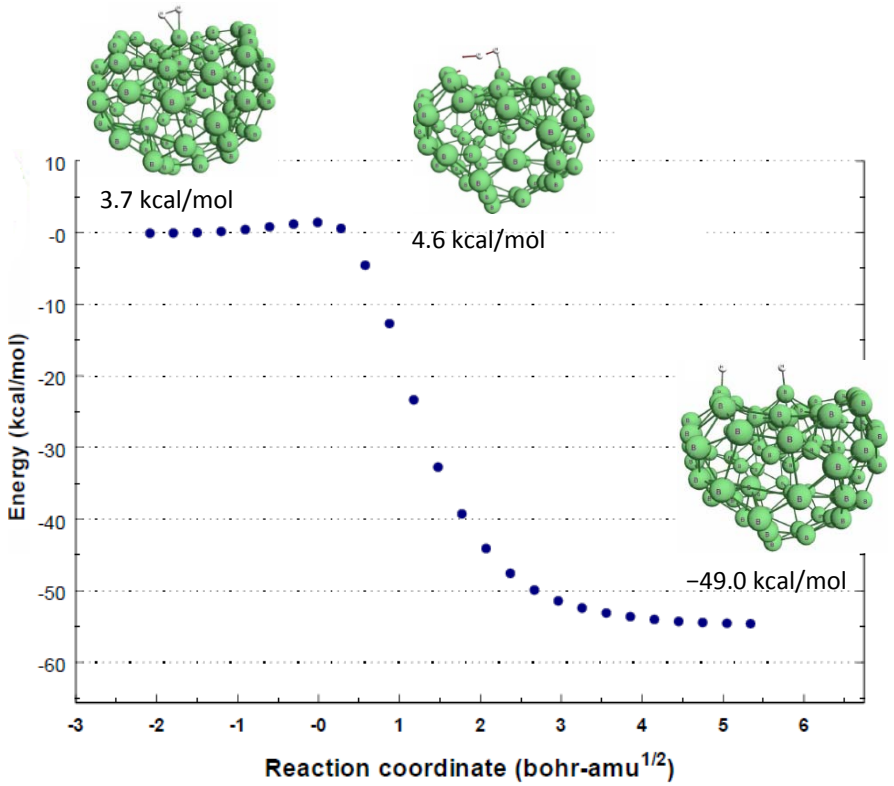

Figure S7. Another reaction pathway for the migration of H atom on the B_{80} surface showing a low activation energy for the formation of a 1,2 product.

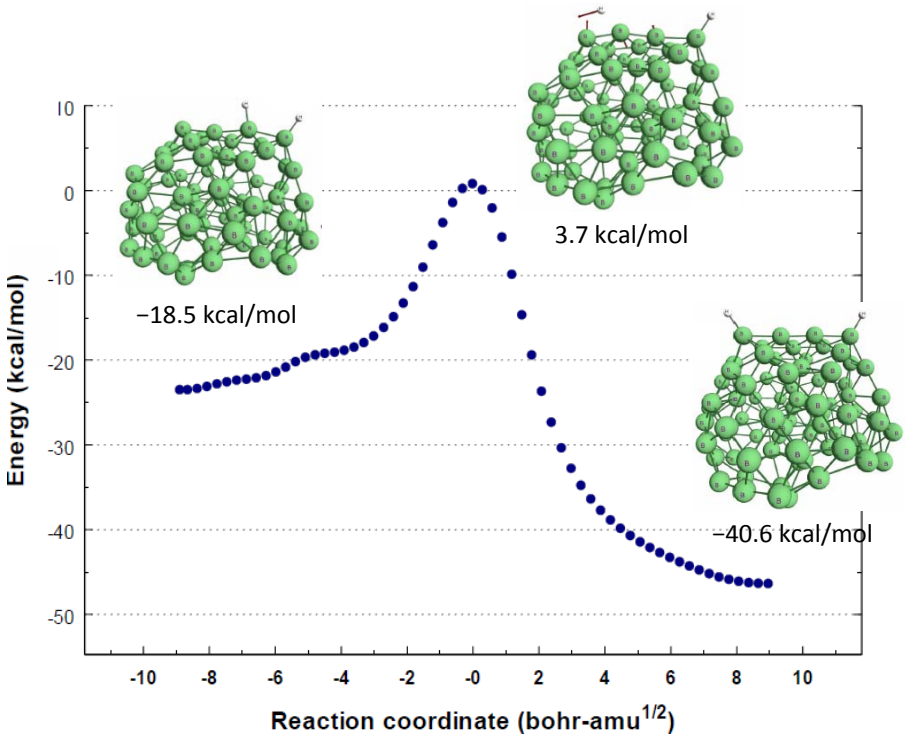

Figure S8. Reaction pathway for the migration of H atom on the B_{80} surface showing formation of a 1,4 B−H complex from a 1,2 complex. The forward barrier for this process is ~22 kcal/mol.

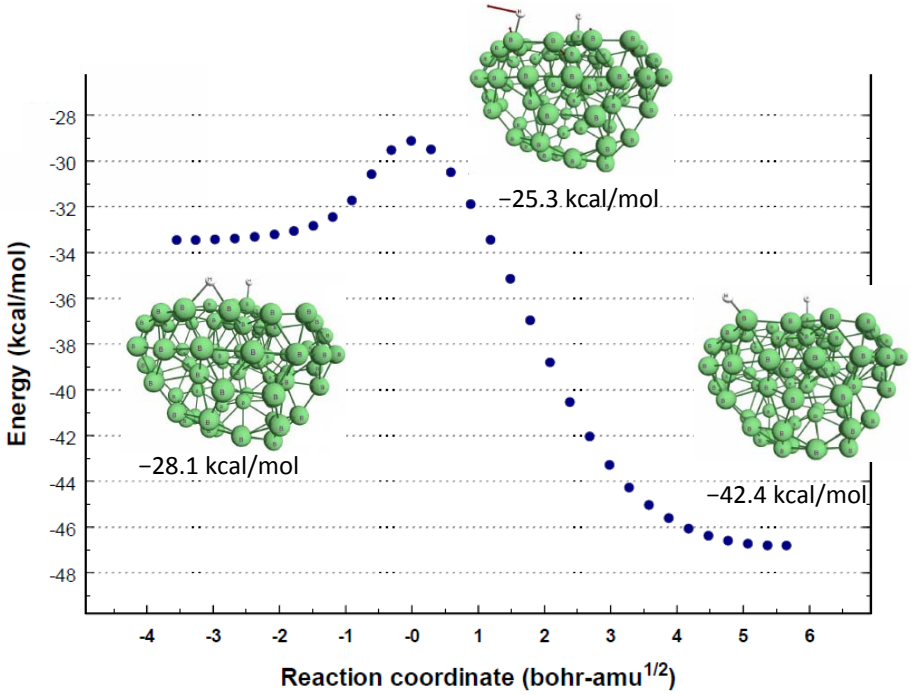

Figure S9. Reaction pathway for the migration of H atom from a B−H−B bridging site to a terminal B−H bond. The energy barrier is ~3 kcal/mol suggesting that bridging hydrogen has a short lifetime at ambient conditions.

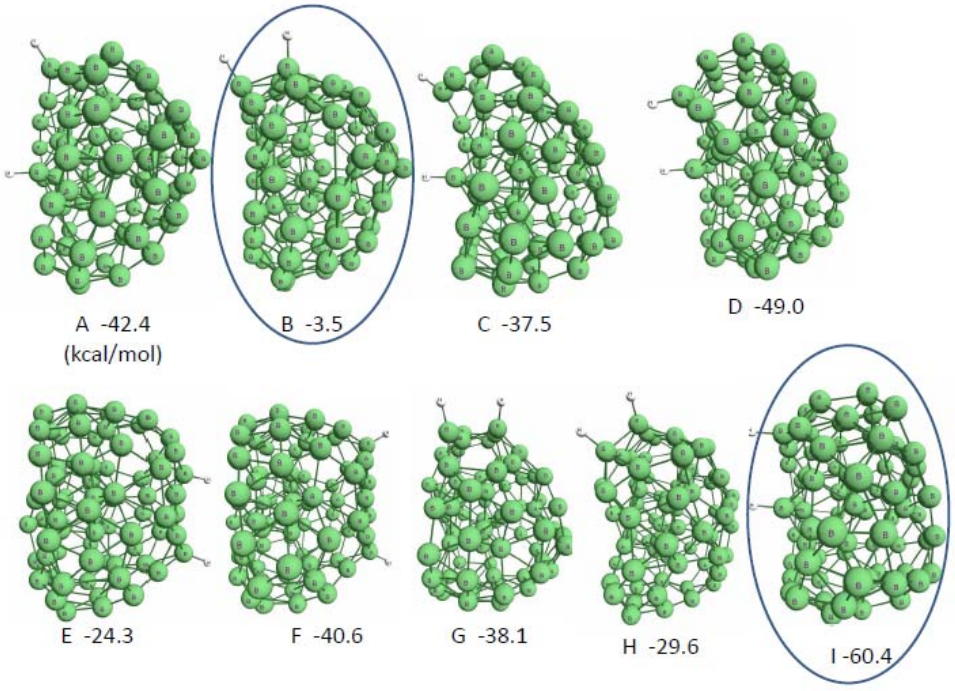

Figure S10. Different isomers of H_2B_{80} with their corresponding enthalpies relative to separated H_2 + B_{80}. The circled structures represent the extremum values obtained from the calculation.

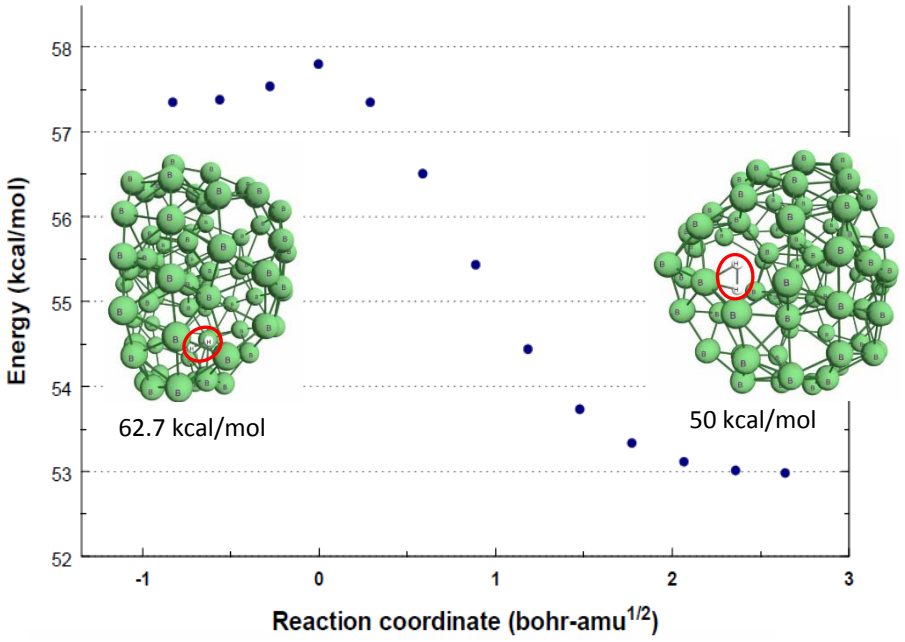

Figure S11. Two views of the M06/6-311+G(d,p) optimized geometry of interstitial H_2 (H_2@B_{80}). The location of the trapped hydrogen molecule is highlighted by a red oval.

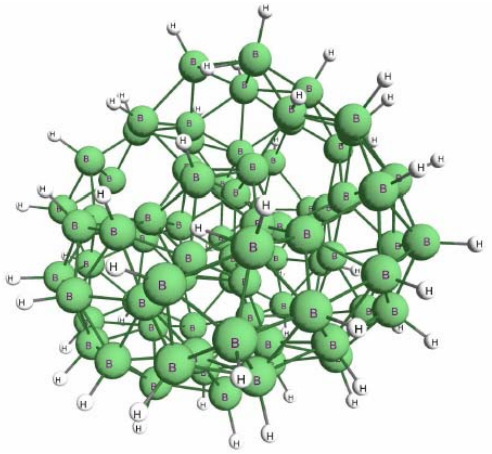

E = −710.3 kcal/mol relative to $29H_2 + B_{80}$

Figure S12. M06/6-311+G(d,p) optimized geometry of $H_{58}B_{80}$

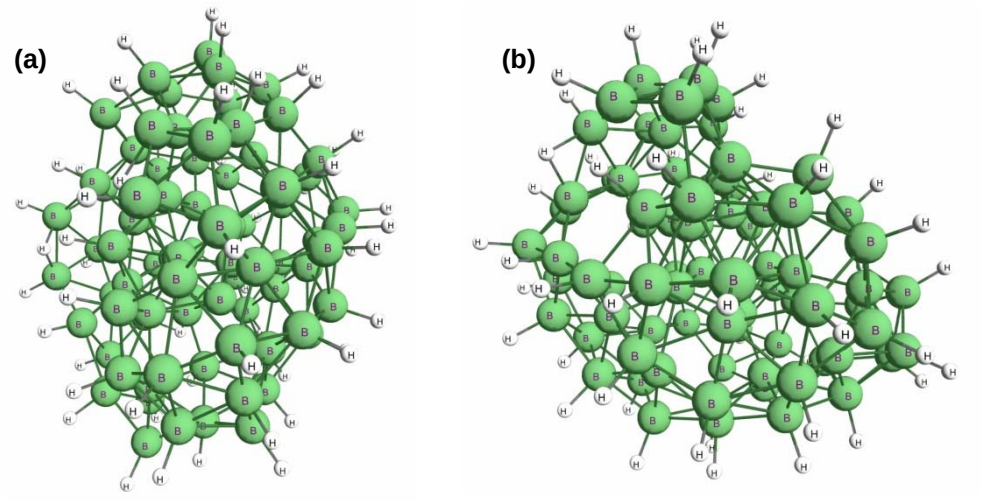

Figure S13. Two views of the M06/6-311+G(d,p) optimized geometry of $H_{60}B_{80}$

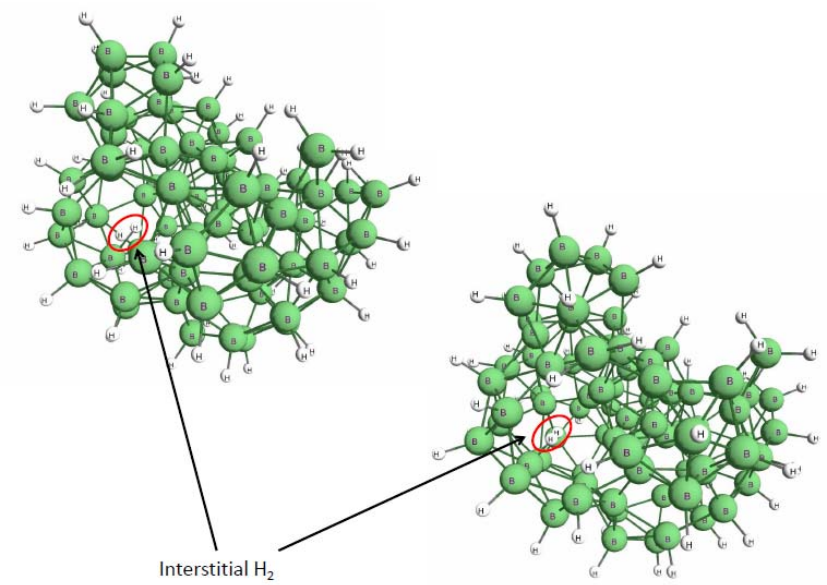

Figure S14. Two views of the M06/6-311+G(d,p) optimized geometry of $H_2@H_{58}B_{80}$. This structure is 74.2 kcal/mol less stable than $H_2 + H_{58}B_{80}$. Moreover, it is unstable with respect to dissociation of the interstitial H_2 to form $H@H_{59}B_{80}$, which is still 28 kcal/mol above the energy of $H_2 + H_{58}B_{80}$.

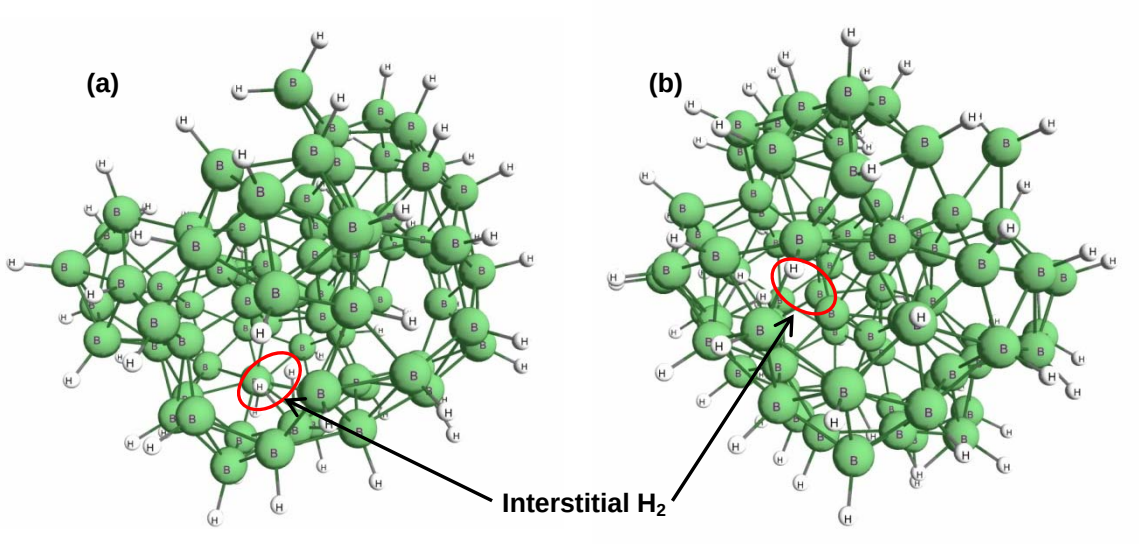

Figure S15. Two views of the M06/6-311+G(d,p) optimized geometry of $H_2@H_{60}B_{80}$. The location of the trapped hydrogen molecule is highlighted by a red oval.

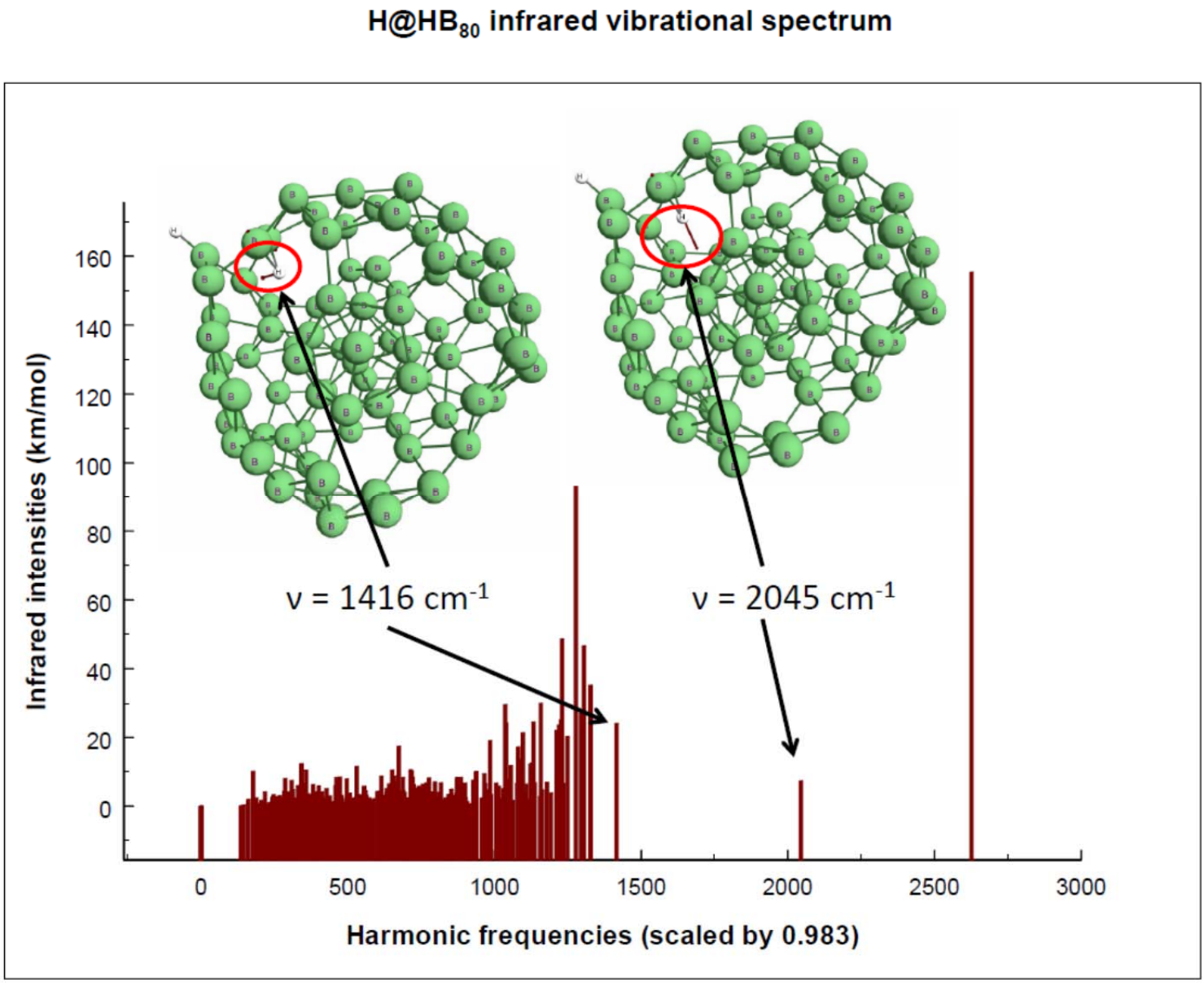

Figure S16. Calculated infrared spectrum of B_{80} with one external and one interstitial H atom. The dense band between ~200 cm^{-1} and 1300 cm^{-1} is due to skeletal vibrations of the B_{80} cage. The two frequencies associated with asymmetric (1416 cm^{-1}) and symmetric (2045 cm^{-1}) stretching motion of the bridging interstitial H are indicated. The arrows drawn on the structures indicate the vibrational displacement vector of the corresponding harmonic frequency. The strong high frequency line at 2627 cm^{-1} is the B-H stretch of the external H atom.

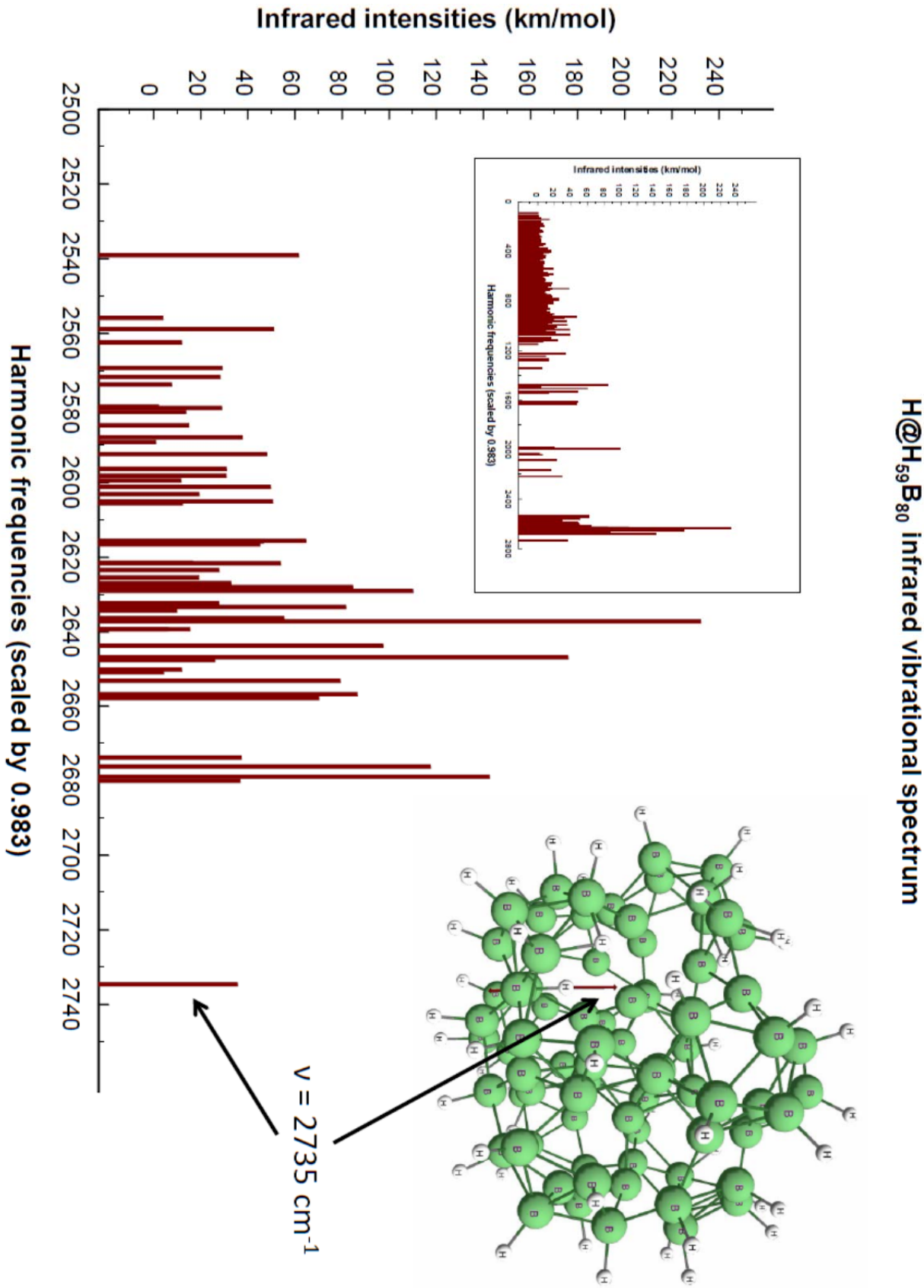

Figure S17. Calculated infrared spectrum of $H@H_{59}B_{80}$. The inset shows the entire spectrum, and the main frame focuses on the B-H stretch region, with the stretch of the interstitial H atom indicated.

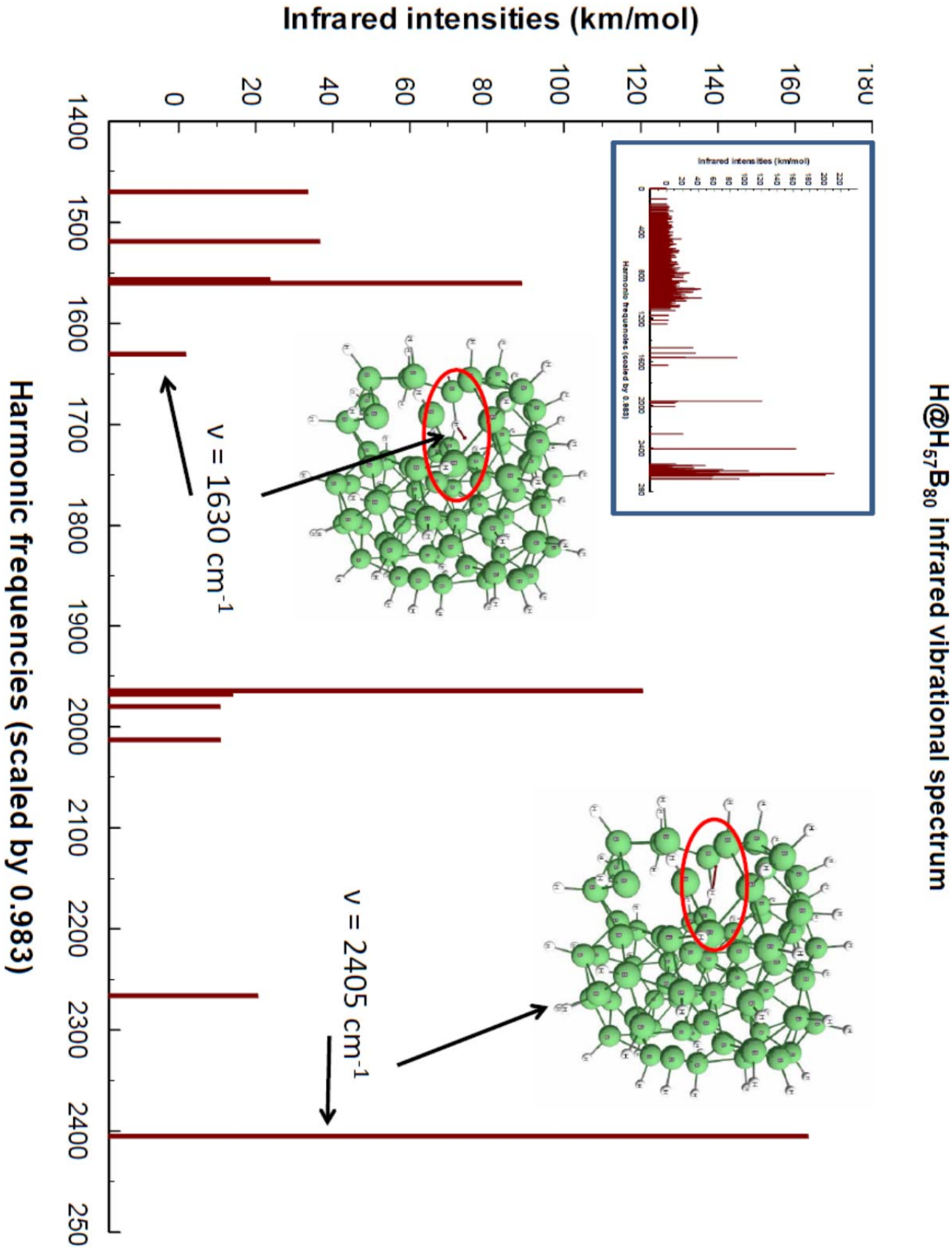

Figure S18. Calculated IR spectrum of $H@H_{57}B_{80}$. The inset shows the entire spectrum, and the main frame focuses on the B-H stretch and bend regions, with the asymmetric and symmetric vibrations of the bridge-bonded interstitial H atom indicated.

Detection and Removal of Contaminants from Boron Feedstock

As shown in Figure 7 of the paper, D_2-milled boron nanoparticles heated under vacuum evolve significant amounts of water and hydrocarbons. To see if these contaminants originated in from the boron feedstock, or were somehow introduced in the milling/handling process, we did similar mass spectrometry experiments on the unmilled feedstock. 95 % purity boron powder is usually obtained from the reduction of B_2O_3 using magnesium metal. Excess magnesium is removed from the reduced boron by dissolving with a strong acid, usually HCl.[4] **Figure S19** shows the mass spectrum of the gases evolved from the feedstock as its temperature was slowly ramped to 400 °C, while continuously leaking the gases into the mass spectrometer, and taking periodic spectra. It can be seen that water, hydrocarbon and other organic compounds are clearly evolved in significant quantities from the feedstock. In addition, signal for H_2^+ is observed, which may include contributions from H_2 evolving from the sample, but also includes contributions from dissociative ionization of water and the hydrocarbons.

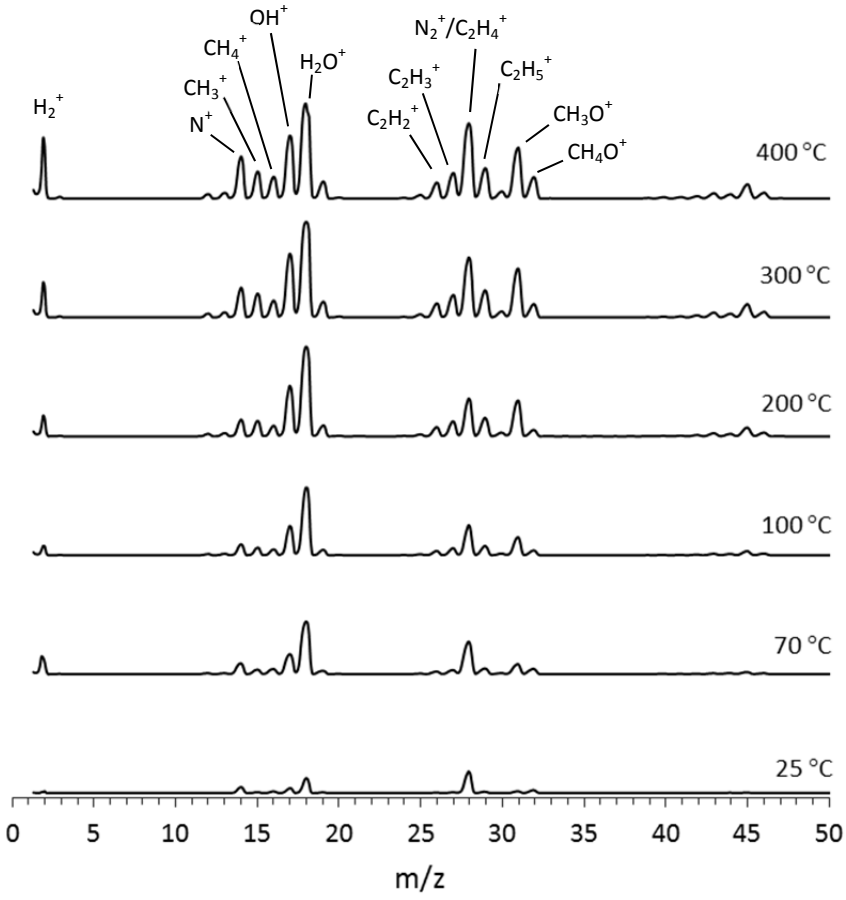

Figure S19. Mass spectra of evolved gases from boron feedstock heated to 400 °C.

One obvious question is whether vacuum heating might be an efficient means to decrease the contaminant level in the feedstock. **Figure S20** compares mass spectra obtained from the same sample at 400 °C during the initial heat ramp (i.e., the final spectrum in **Figure S19**), and after heating under vacuum at 400 °C for 12 hours, followed by cooling to room temperature and then heating back to 400 °C. It can be seen that the water and organic ion signals are essentially absent in the spectrum of the de-gassed sample. Curiously, there is still substantial H_2^+ signal after de-gassing, raising the possibility that there is some background source of hydrogen in the experiment at high temperature, such as diffusion of hydrogen through the wall of the glass sample tube.

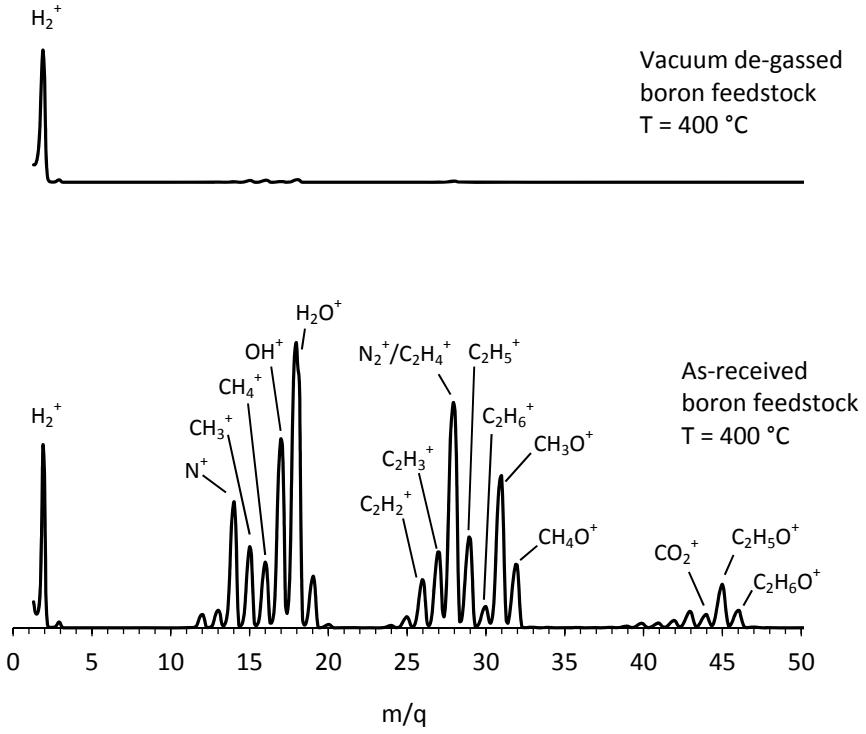

Figure S20. Mass spectrum of gases evolved from 95 % boron feedstock after cleaning overnight via heating under vacuum (top). Mass spectrum of as received boron 95 % boron feedstock (bottom). Samples were heated at 400 °C to enhance gas desorption.

Ignition Tests on H_2-Loaded Boron Nanoparticles Dispersed in Hypergolic Ionic Liquids

Ignition tests were conducted on neat ILs and with H2-loaded boron nanoparticles dispersed in them. **Figures S21 – S24** show the results of these measurements.

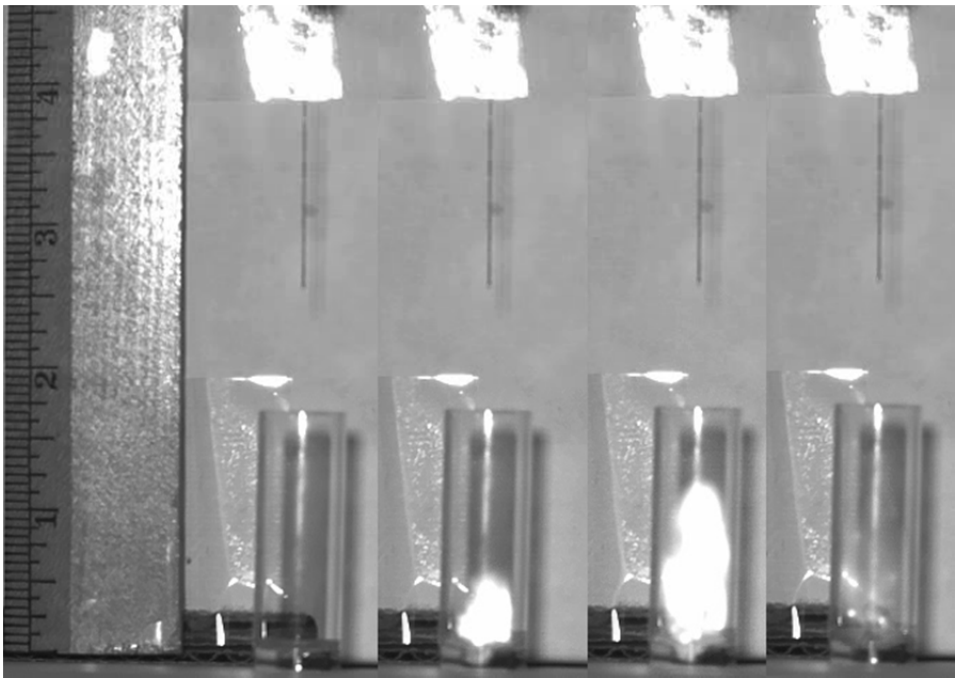

Figure S21. Hypergolic drop test of a sample of neat [BMIM][DCA] displaying a very weak ignition: (from left to right) 0 ms – drop of IL hitting the surface of the nitric acid, 40 ms – initial sign of ignition, 41 ms – largest flame height observed, and 46 ms – final stages of ignition

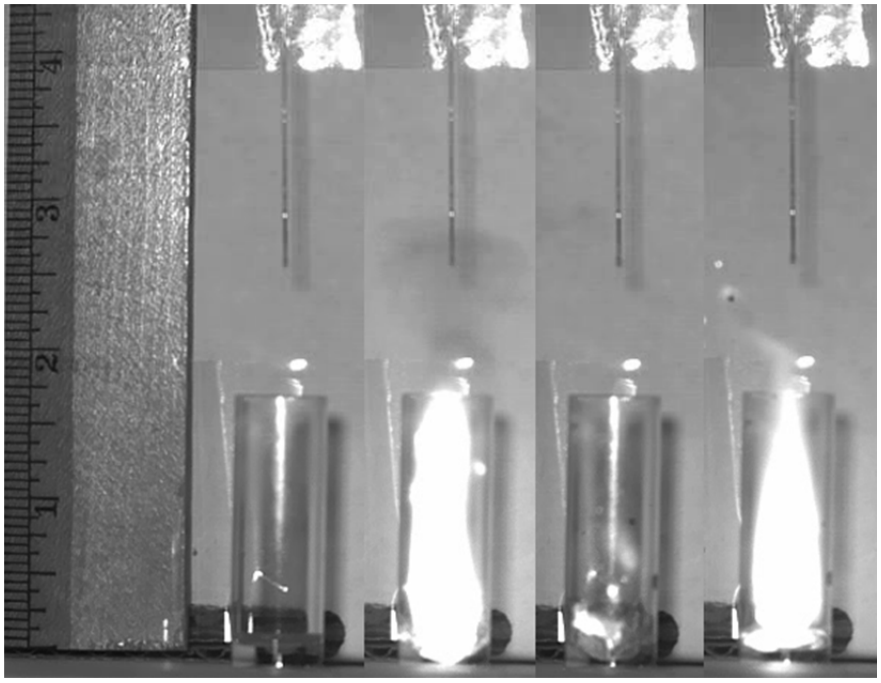

Figure S22. Hypergolic drop test of [BMIM][DCA] with 0.3 wt% of boron nanoparticles displaying an improved flame height, but an intermittent combustion: (from left to right) 0 ms – drop of IL hitting the surface of the nitric acid, 46 ms – largest flame observed in first ignition, 128 ms – first ignition ceases, and 194 ms – largest flame obtained in second ignition

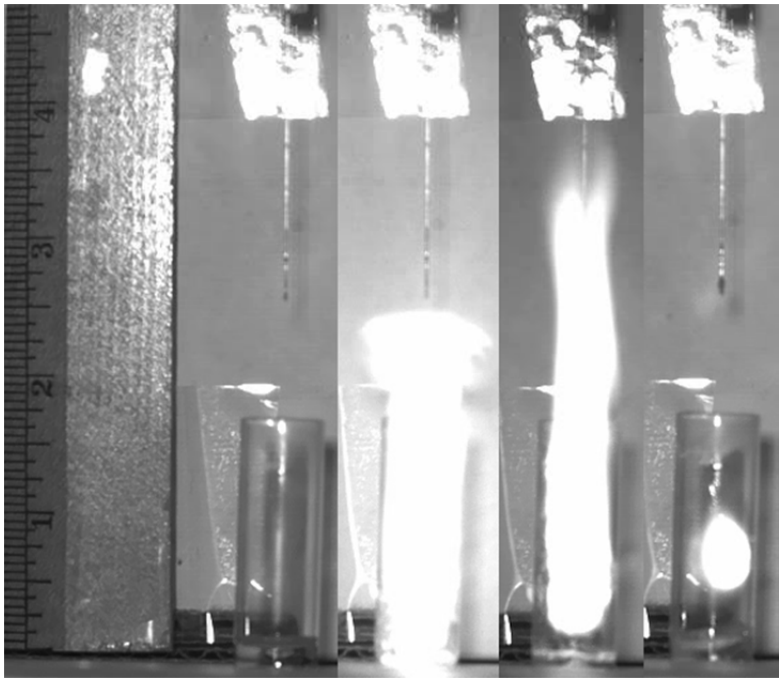

Figure S23. Hypergolic drop test of a sample of neat [MAT][DCA] displaying a moderate ignition: (from left to right) 0 ms – drop of IL hitting the surface of the nitric acid, 44 ms – shortly after ignition, 74 ms – largest flame height observed, and 158 ms – final stages of ignition.

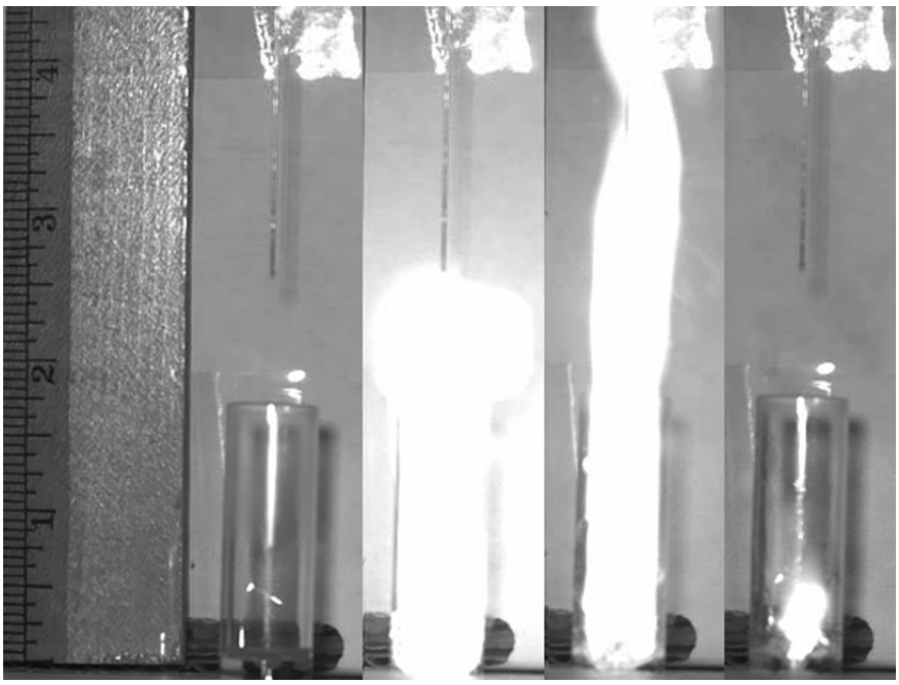

Figure S24. Hypergolic drop test of a sample of [MAT][DCA] with 0.3% wt boron nanoparticles displaying a performance increase: (from left to right) 0 ms – drop of IL hitting the surface of the nitric acid, 34 ms – initial sign of ignition, 78 ms – largest flame height observed, and 100 ms – final stages of ignition.

References

(1) Linstrom, P. J.; Mallard, W. G., NIST Chemistry WebBook, NIST Standard Reference Database Number 69. National Institute of Standards and Technology: Gaithersburg MD, 20899, 2011.

(2) Haynes, W. M., *CRC Handbook of Chemistry and Physics*. 94th ed.; CRC Press Taylor and Francis Group: Boca Raton, FL, 2013.

(3) Powell, C. J.; Jablonski, A., *NIST Electron Effective Attenuation Length Database Version 1.3*. Gaithersburg, MD, 2003.

(4) Markovskii, L. Y., *Electron Technology* **1970,** *3*, 95-102.

(5) Zhao, J.; Wang, L.; Li, F.; Chen, Z., *J. Phys. Chem. A* **2010,** *114*, 9969-9972.

(6) Li, F.; Jin, P.; Jiang, D.; Wang, L.; Zhang, S. B.; Zhao, J.; Chen, Z., *J. Chem. Phys.* **2012,** *136*, 074302-074311.

(7) Schmidt, M. W.; Gordon, M. S.; Dupuis, M., *J. Am. Chem. Soc.* **1985,** *107*, 2585-2589.

(8) Muller, K., *Angew. Chem., Int. Ed. Engl.* **1980,** *19*, 1-13.

(9) Ishida, K.; Morokuma, K.; Komornicki, A., *J. Chem. Phys.* **1977,** *66*, 2153-2156.

(10) Gonzalez, C.; Schlegel, H. B., *J. Chem. Phys.* **1989,** *90*, 2154-2161.

(11) Garrett, B. C.; Redmon, M. J.; Steckler, R.; Truhlar, D. G.; Baldridge, K. K.; Bartol, D.; Schmidt, M. W.; Gordon, M. S., *Journal of Physical Chemistry* **1988,** *92*, 1476-1488.

(12) Baldridge, K. K.; Gordon, M. S.; Steckler, R.; Truhlar, D. G., *Journal of Physical Chemistry* **1989,** *93*, 5107-5119.